Searches for Di-Higgs Production in the $b\bar{b}\gamma\gamma$ Final State with the CMS Run-2 Dataset

Rafael Teixeira de Lima

Northeastern University

Boston - Massachusetts

A thesis submitted for the degree of

Doctor of Philosophy

April, 2017

This thesis is dedicated to
someone
for some special reason

Acknowledgements

plenty of waffle, plenty of waffle, plenty of waffle, plenty of waffle, plenty of waffle, plenty of waffle, plenty of waffle, plenty of waffle.

Abstract

plenty of waffle, plenty of waffle, plenty of waffle, plenty of waffle, plenty of waffle, plenty of waffle, plenty of waffle, plenty of waffle.

Contents

Chapter 1

Introduction

Lorem ipsum dolor sit amet, consectetur adipiscing elit, sed do eiusmod tempor incididunt ut labore et dolore magna aliqua. Ut enim ad minim veniam, quis nostrud exercitation ullamco laboris nisi ut aliquip ex ea commodo consequat. Duis aute irure dolor in reprehenderit in voluptate velit esse cillum dolore eu fugiat nulla pariatur. Excepteur sint occaecat cupidatat non proident, sunt in culpa qui officia deserunt mollit anim id est laborum.

1.1 The Standard Model of Particle Physics

1.2 Higgs Physics Current Status

1.3 Higgs as a Probe to New Physics

Einstein's paper: [**?**]

Chapter 2

The Large Hadron Collider and the Compact Muon Solenoid Experiment

Lorem ipsum dolor sit amet, consectetur adipiscing elit, sed do eiusmod tempor incididunt ut labore et dolore magna aliqua. Ut enim ad minim veniam, quis nostrud exercitation ullamco laboris nisi ut aliquip ex ea commodo consequat. Duis aute irure dolor in reprehenderit in voluptate velit esse cillum dolore eu fugiat nulla pariatur. Excepteur sint occaecat cupidatat non proident, sunt in culpa qui officia deserunt mollit anim id est laborum.

2.1 The LHC Accelerator Complex

2.2 The CMS Experiment

2.2.1 The CMS Tracking Detectors

2.2.2 The CMS Calorimetry Detectors

2.2.3 The CMS Muon Detectors

2.2.4 The CMS Trigger and Data Acquisition Systems

2.2.5 Object Reconstruction at CMS

2.2.5.1 Photons and Electrons

2.2.5.2 Jets

2.2.5.3 Muons

2.2.5.4 Identification of b-quark jets

Einstein's paper: [?]

Chapter 3

The CMS Electromagnetic Calorimeter

The CMS ECAL is a high-resolution, hermetic, and homogeneous electromagnetic calorimeter made of 75,848 scintillating lead tungstate crystals divided among a barrel ($|\eta| < 1.48$) and two endcaps ($1.48 < |\eta| < 3.0$) [**?**]. These crystals are characterized by fast light emission (80% of light emitted in 25 ns), short radiation length ($X_0 = 0.89$ cm) and small Moliere radius ($R_M = 2.10$ cm). The light emitted by these crystals is detected with avalanche photodiodes (APDs) in the barrel and vaccuum photontriodes (VPTs) in the endcaps. The signal readout is performed with two avalanche photodiodes (APDs) per crystal in the barrel, and one vacuum phototriode (VPT) in the endcaps. These characteristics, translated into precise energy and timing resolutions, are an invaluable tool for the CMS physics program.

Completing the CMS electromagnetic calorimeter system is a preshower detector (ES), based on lead absorbers equipped with silicon strip sensors. It is installed in front of the ECAL endcaps, covering the region $1.65 < |\eta| < 2.6$. The fine granularity of the ES strips (2 mm wide) can resolve the signals of high-energy photons from the decays of neutral pions into two photons, when the separation angle between the photons is small, and can determine precisely the position of the electromagnetic deposits.

During the first year of Run II data taking at 13 TeV, the LHC provided a challenging environment, with one bunch crossing every 25 ns and an average of 10 interactions per crossing (pile up). This is expected to be even more challenging in 2016, with up to 40 pile up interactions. In the 2015 data taking period, the CMS ECAL operated with more than 98% of its channels active, and was responsible for less than 7% of CMS downtime during physics runs.

3.1 Detector Components

3.1.1 $PbWO_4$ Crystals and In-detector Electronics

3.1.2 Trigger and Data Acquisition Systems

3.2 Electron and Photon Energy Reconstruction

The photon and electron energy reconstruction based on ECAL energy deposits is based on the formula: $E_{e,\gamma} = [\sum_i (S_i(t) \times c_i \times A_i) \times G(\eta) + E_{ES}] \times F_{e,\gamma}$, with A_i, c_i and $S_i(t)$ as, respectively, the per individual channel amplitude, intercalibration constant and light monitoring constant, $G(\eta)$ is the ADC to GeV absolute scale, E_{ES} is the energy deposit in the preshower, and $F_{e,\gamma}$ are the cluster corrections (different for photons and electrons). These terms will be detailed in the next sections.

3.2.1 Online Reconstruction

The online reconstruction of ECAL deposits starts with the amplification and digitization of the signal from the photodetectors attached to the crystals. This is performed by a multi-gain preamplifier (MGPA), and a 12 bit ADC running at 40 MHz. Ten consecutive samples are recorded and used to perform the pulse reconstruction and amplitude extraction.

The time spacing between two consecutive samples from the ECAL readout electronics is 25 ns, which is the same time spacing between two colliding bunches in the LHC. This implies that, during the readout of one pulse, another scintillation process might start in the same crystal, compromising the in-time amplitude reconstruction. To mitigate this effect, also called out-of-time (OOT) pile up, a new online pulse reconstruction method (multifit) was developed to replace the Run I method [?].

In the multifit method, the pulse shape is reconstructed based on a fit to the time samples, minimizing $\chi^2 = \sum_{i=1}^{10} \left(\sum_j^M A_j p_{ij} - S_i \right)^2 / \sigma_{S_i}^2$. The samples ($S_i$) are fitted with one in-time pulse shape template, plus up to 9 out-of-time templates (p_{ij}) times their respective amplitudes (A_j). σ_{S_i} is noise generated by electronics associated with the crystal readout chain. The OOT templates have the same shape as the in time one, but are shifted in time by multiples of 1 bunch crossing (1 BX = 25 ns), within a range of -5 to +4 BX around the in time signal (BX = 0). The pulse shapes have been measured in early 2015, in special runs in which the LHC delivered isolated bunches (no OOT pile up).

It has been observed in both data and simulation that, with the multifit method, OOT pile up reconstruction is negligible. The energy resolution improvement, with respect to the Run I amplitude reconstruction method, is substantial especially for low E_T photons and electrons, given the larger contribution of deposits from pile up to the total energy.

3.2.2 Response Monitoring

Time dependent corrections must be applied to the reconstructed amplitude due to changes in detector response with radiation exposure. These changes in response are due to decreases in crystal transparency and variations in VPT response in endcaps.

The changes in the crystal transparency is due to ionizing radiation creating color centers in the lead tungstate. While the scintillation process remains intact, the amount of light detected by the photodetectors decreases. This effect is partially mitigated through thermal annealing, causing the transparency to increase in the absence of radiation.

A light monitoring system is used to monitor the overall changes in response in the ECAL [**?**]. It consists of a system of lasers (operating at 447 nm, close to the wavelength of peak emission for lead tungstate) that injects light in each ECAL crystal, which is then read by the standard ECAL readout. The difference between input and read laser amplitudes are then used to calculate correction factors.

The history of response change measurements is summarized in Figure 3.1. The changes are up to 6% in the barrel and reach up to 30% at $|\eta| \approx 2.5$, the limit of the tracker acceptance. For high $|\eta|$ regions, changes are up to 70%. The recovery of the crystal response during the long shutdown period is visible. The response was not fully recovered, however, particularly in the region closest to the beam pipe. The monitoring corrections are validated by comparing isolated electron energy as measured by ECAL (E) and momentum as measured by the CMS Tracker (p), before and after light monitoring corrections. It is seen that the measured corrections bring stability to energy measurements with ECAL.

Figure 3.1: History of channel response changes as measured by the light monitoring system.

Figure 3.2: ECAL energy resolution measured with $Z \rightarrow ee$ events for low bremsstrahlung electrons in the ECAL barrel.

3.2.3 Intercalibration

A relative calibration procedure in all ECAL channels is performed to ensure uniformity across the detector. Different and independent methods are used to calculate intercalibration constants (ICs), which are then combined to achieve the desired precision of $< 0.5\%$. The final 2015 version of the ICs have been calculated with the full 2.6 fb^{-1} dataset recorded by CMS with B=3.8 T. The following methods are the same as in Run I [**?**].

The ϕ-symmetry method is based on the expected uniformity of the energy flux along ϕ rings (region with fixed η). The ICs are calculated to correct non-uniformities in this flux. This method was used in 2015 to translate the latest ICs, calculated with the full 2012 dataset, to the 2015 detector conditions. This was done by scaling the 2012 ICs by the ratio between 2015 and 2012 ϕ-symmetry ICs. The π^0/η method consists of measuring the invariant mass of these resonances' decays to two photons and maximizing their resolutions by varying the ICs iteratively. The E/p method employs the same logic as the light monitoring validation method, comparing isolated electron energy and momentum. An iterative method is used to minimize the spread of the E/p distribution. The combined intercalibration was obtained from the mean of the individual ICs at a fixed value of η, weighted by their respective precisions. The residual miscalibration of an intercalibration method, which is related to the final method precision, is calculated as the spread of the difference between the method's ICs and the other methods' ICs at a fixed value of η. The combination of ICs achieves the desired goal of less than 0.5% precision.

3.2.4 Absolute Calibration

$Z \to ee$ events are used both to set the η scale and the absolute calibration [**?**]. The first is developed to ensure that different η regions have the same relative response, while the second (done separately for barrel and endcaps) sets the absolute energy scale.

A dedicated calibration was performed with 0 T data to account for differences in shower shapes in the absence of magnetic field. For example, in 0 T there is no bremsstrahlung radiation outside the main electron cluster deposit, improving the reconstructed energy resolution.

In addition, the calibration was validated with high energy photons and electrons. The validation was performed by comparing data and Monte Carlo simulations for high energy electrons from $Z \to ee$. The calibration was found to be stable to 0.5%

(0.7%) for electrons up to $p_T = 150$ GeV in the barrel (endcap). Possible saturation effects were corrected for with a multivariate technique, but those effects were found to be $< 2\%$ for photons arriving from resonance masses less than 1.4 TeV.

3.2.5 High Level Calibrations

The amount of material in front of ECAL, up to $2X_0$ in the barrel outer regions, produces a high rate of bremsstrahlung radiation from electrons and a high probability of photon conversions. To mitigate this effect, a clustering algorithm is used to recombine energy deposits that come from those processes. The cluster energy is corrected via a multivariate technique, separately for photons [?] and electrons [?]. It also aims to correct other effects, such as in time pile up.

3.3 ECAL Performance with Run II data

The ECAL energy resolution is measured using $Z \rightarrow ee$ events, from an unbinned fit with a Breit-Wigner function convoluted with a Gaussian as signal model. Degradation effects come from the amount of material in front of ECAL and cracks between modules. The resolution, as a function of η, for low bremsstrahlung electrons in the barrel can be seen in Figure 3.2. The energy resolution achieved using the latest 2015 calibration constants is less than 2% for low bremsstrahlung electrons in the barrel.

3.3.1 Performance

3.4 The CMS ECAL Barrel Upgrade

Einstein's paper: [?]

Chapter 4

Exotic Higgs Decays in γ+MET Final States

Lorem ipsum dolor sit amet, consectetur adipiscing elit, sed do eiusmod tempor incididunt ut labore et dolore magna aliqua. Ut enim ad minim veniam, quis nostrud exercitation ullamco laboris nisi ut aliquip ex ea commodo consequat. Duis aute irure dolor in reprehenderit in voluptate velit esse cillum dolore eu fugiat nulla pariatur. Excepteur sint occaecat cupidatat non proident, sunt in culpa qui officia deserunt mollit anim id est laborum.

4.1 Run-1 CMS $H \to \gamma$+MET Analysis

4.2 $H \to \gamma\gamma$+MET Projection Studies

Einstein's paper: [?]

Chapter 5

HH searches with photons and b-jets at CMS Run 2

5.1 Introduction

This Analysis Note describes the inclusive search for the double Higgs production process in the decay mode HH $\rightarrow b\bar{b}\gamma\gamma$ at $\sqrt{s} = 13\,\text{TeV}$, with 36.5 fb^{-1} from the 2016 data taking period. This analysis is based on the search at 8 TeV performed in the same final state, recently published by CMS in Ref. [?] (the internal CMS documentation of this analysis can be found in Refs. [?, ?]), and on the earlier 13 TeV search using 2015 data HIG-16-032.

Many theories beyond the SM (BSM) suggest the existence of new physics potentially manifested in the detection of a pair of Higgs bosons. The simplest signal we can look for is in the form of a resonant contribution to the invariant mass of the HH system (resonant search). If the BSM new particles are not directly detectable (either too heavy or too light to be in the HH invariant mass spectrum), but still couple to HH, their virtual contribution to the non-resonant HH production can still be measured (as shown, e.g., in Refs. [?, ?]). Additionally, the fundamental couplings of the Higgs boson to other SM particles (including itself) can be modified as well in BSM theories (as shown, e.g., in Refs. [?, ?]). Both of these cases can be studied via the non-resonant HH process.

In order to study the HH production, the Higgs bosons' final states must be carefully chosen. On one hand, the overall cross section of the process must be kept high enough for a good sensitivity. On the other hand, a good selection efficiency, online and offline, is important for a well performing analysis. This is achieved with the $b\bar{b}\gamma\gamma$ final state. The H $\rightarrow b\bar{b}$ leg provides a high branching ratio (57.7%), while the H $\rightarrow \gamma\gamma$ leg provides an efficient way to correctly identify the interesting events and a high mass resolution. The total branching ratio of the HH $\rightarrow b\bar{b}\gamma\gamma$ channel is 0.26%.

The resonant analysis is dedicated to the search of a generic narrow width resonance (both spin-0 and spin-2). In this note, we will use a Warped Extra Dimensions (WED) theory[1] as a benchmark model for resonant HH search. It provides candidates for both spin-0 (radion) and spin-2 (graviton[2]) that decay into HH.

In the non-resonant search, we investigate explicitly the case of anomalous couplings in the Higgs boson potential, following the same model parametrization used in Ref. [?]. In the 13 TeV analysis however we study the parameter space of anomalous couplings using the approach suggested in [?], where physics benchmarks are defined based in basic signal kinematics. We also put limits in the Standard Model like HH production, a process that has a cross section of $\sigma_{HH}(SMNNLO) = 33.70$ fb at 13 TeV [?].

This note is organized as follows. In section 5.2, we describe the data and Monte Carlo samples used in the analysis, both for signal and background. In section 5.3.1, the online selection used in this analysis is described. Sections 5.3.2 and 5.3.3 are dedicated to the object reconstruction and selection in the analysis. The categorization procedure for the resonant and non-resonant analyses is defined in section 5.8.2 Section 5.5 described a new variable $\tilde{M}_{\mathrm{X}}$ that is a better proxy to the true 4-body invariant mass than the standard $M(jj\gamma\gamma)$, and how it is used to create signal mass dependent selections. The selection efficiencies are shown in section 5.6. The limits and signal extraction are defined in section 5.8, along with the signal and background modeling procedures. The systematic uncertainties for this analysis are defined in section 5.9. Finally, the results are shown in sections 5.10 and 5.11, for the resonant and non-resonant analyses respectively. Section 5.12 provides a summary of this analysis note.

5.1.1 Strategy Summary

The main strategy upgrades with respect to the Run-I analysis are:

- We make use of MVA ID for the photon selection, which improves the selection efficiency, see section 5.3.2

[1] Based in the Randall-Sundrum (RS) setup [?].

[2] The graviton can be interpreted either as the first Kaluza-Klein (KK) excitation, or the graviton in the bulk RS scenario [?, ?, ?]

- Using $\tilde{M}_{\mathrm{X}}$ variable instead of 4-body mass, $M(jj\gamma\gamma)$. This allows to cancel the effects of the low dijet mass resolution (compared to $M(\gamma\gamma)$). uncertainties in the jet energy scale, see Section 5.5

- An improved version of the Combined Secondary Vertex algorithm (CSVv2) for b-tagging was developed in CMS.

- A new categorization method was developed to deal with signal categories and phase spaces with not enough events for a reliable background description.

- A dedicated b-jet energy regression is being developed for Run-II analysis, see Section 5.3.3.1.

- The main part of the analysis is performed in a framework based on top of the one developed by the $\mathrm{H} \to \gamma\gamma$ group [**?**], so we benefit from the latest and greatest photon selection tools available.

In the new version of the analysis we also profit from a better description of the signal in the MC samples (Section 5.2), and a higher statistics of the MC events. The description of the simulated background is also improved. We observe a good agreement in the shapes of the basic distributions between data and MC in all control regions, see Section 5.7.

There are however a few new challenges in Run-II analysis. We utilize the double-photon trigger to select event for the analysis. Compared to the 8 TeV data-taking the E_T thresholds of the L1 seeds of those triggers were increased, which reduces the selection efficiency of the signal. Smaller distance parameter in the jet clustering algorithm is used by CMS ($D = 0.4$ in Run-II vs $D = 0.5$ in Run-I), which introduces a larger bias and decreased resolution in the reconstruction of the $M(jj)$ variable. Another challenge of the CMS running conditions in Run-II is higher pile-up environment, specially during the 2016 data taking.

With respect to the 2015 version of the analysis, many improvements have been implemented focusing on maximizing the S/B, given the larger amount of data available. New categorization schemes have been developed and the mass window selection has been re-optimized. A new training for the b jet energy regression has also been developed, with a better performance both regarding the jet energy scale and resolution.

5.2 Samples

All the MC samples used were processed centrally. As default for CMS, the signal samples use PDF4LHC15_nlo_mc_pdfas set [?, ?, ?, ?, ?] in the four flavour scheme. The central value for the strong coupling is taken as $\alpha_s(m_Z) = 0.118$. This analysis aims to investigate data collected by CMS in 2016, therefore, all the samples mentioned below have been produced in the 80X CMSSW releases. The samples used in this analysis have also been pre-processed by the central H $\rightarrow \gamma\gamma$ analysis framework FLASHgg, in order to obtain and latest and greatest photon energy, resolution and ID used by the SM main analysis.

5.2.1 Signal MC: resonant production

To simulate the generic resonances we use `MG5_aMC@NLO` [?] at leading order. For the gluon fusion produced spin-2 resonance, we use the model for a KK-graviton in the bulk described on [?], which is an adaptation of the RS1 model of Ref. [?, ?], introducing the relevant coupling modifications. The model files can be found in [?] and its found to agree at the level of cross sections and branching ratios with the bulk WED scenario implemented by the authors of [?] on `CalcHep` [?] framework. To simulate the scalar resonance, we use the Higgs Effective Model [?] that can found in the `Feynrules` database [?].

The spin-0 and spin-2 resonances are simulated with masses: 250, 260, 270, 280, 300, 320, 340, 350, 400, 450, 500, 550, 600, 650, 700, 750, 800, 900, 1000 GeV, with 50K events each, assuming resonance width of 1 GeV. The samples corresponding to each signal point are:

- Spin-0: `/GluGluToRadionToHHTo2B2G_M-XXX_narrow_13TeV-madgraph`
- Spin-2: `/GluGluToBulkGravitonToHHTo2B2G_M-XXX_narrow_13TeV-madgraph`

The cross sections for the interpretations can be found here [?]. The `MG5_aMC@NLO` configuration cards used for the simulations are organized here [?].

5.2.2 Signal MC: nonresonant production

In the SM, Higgs boson pair production occurs predominantly by gluon-gluon fusion (GF) via an internal fermion loop. Since the Higgs boson couplings are defined by the particles masses, the top quark contribution is dominant, while couplings to light quarks are negligible [3]. In the absence of new light states, the GF Higgs boson pair production at the LHC can then be generally described (to leading approximation) by five parameters controlling the tree-level interactions of the Higgs boson. The Higgs boson trilinear coupling and the top Yukawa interaction exist in the SM Lagrangian, where the former is given by $\lambda_{SM} = m_h^2/2v^2$, with v the vacuum-expectation value of the Higgs field. Deviations from SM values are parametrized with the multiplicative factors κ_λ and κ_t, respectively. The contact interactions of the Higgs boson with gluons and those coupling two Higgs bosons with two gluons or a top-antitop quark pair, which could arise through the mediation of very heavy new states, are instead genuinely not predicted by the SM; they can be parametrized by the absolute couplings c_g, c_{2g}, and c_2. The relevant part of the Lagrangian then takes the form

$$\mathcal{L}_h = \frac{1}{2}\partial_\mu h\partial^\mu h - \frac{1}{2}m_h^2 h^2 - \kappa_\lambda\, \lambda_{SM} v\, h^3 - \frac{m_t}{v}(v + \kappa_t\, h + \frac{c_2}{v}\, h\, h)\, (\bar{t_L} t_R + h.c.) + \frac{1}{4}\frac{\alpha_s}{3\pi v}(c_g\, h - \frac{c_{2g}}{2v}\, h\, h)\, G^{\mu\nu} G_{\mu\nu}\,. \quad (5.1)$$

The different Feynman diagrams contributing to a di-Higgs boson signal in pp collisions at leading order (LO) are shown in Fig. 5.1. The simulation setup used in this paper was produced by the authors of [?], we use `MG5_aMC@NLO` as generator. The LO process is already at one-loop level; in the approach followed in [?], loop factors are calculated on an event-by-event basis with a `Fortran` routine on top of an *aMC@NLO* [?, ?] effective model;

In the Ref. [?] it was designed a method to partition the 5 dimensional parameter space in regions with similar LO kinematics. When the simulation was launched in the CMS system this work was in preliminary version, we had simulated the samples referent to the recommendations of its first version. The list of relevant parameters iused in each sample is in table 5.2. The `MG5_aMC@NLO` configuration cards used for the simulations are organized here [?]. Since then, the metric used by the method was improved and the parameter space scan extended, resulting in a new set of benchmarks, that can be found in the last ArXiV version of the mentioned paper, and as well in [?].

The full simulated samples can be found on DAS as:

- `/GluGluToHHTo2B2G_node_X_13TeV-madgraph`

[3] This assumption is motivated also in BSM theories where the Higgs sector is minimal (see also [?])

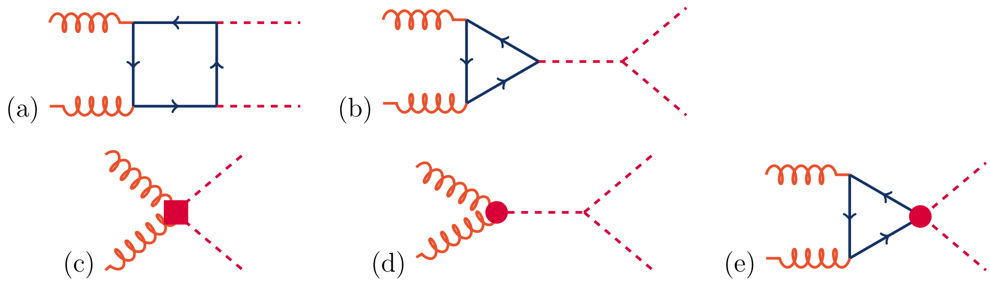

Figure 5.1: Feynman diagrams that contribute to Higgs boson pair production by gluon-gluon fusion at leading order. Diagrams (a) and (b) correspond to SM-like processes, while diagrams (c), (d), and (e) correspond to pure BSM effects: (c) and (d) describe contact interactions between the Higgs boson and gluons, and (e) exploits the contact interaction of two Higgs bosons with top quarks.

where the X ranges between 0 and 13. The $X = 0$ represents the point (κ_λ, κ_t, c_2, c_g, c_{2g}) = (0,1,0,0,0) - when the process is induced only by the box diagram and the reminiscent correspond to the points listed in Tab. 5.2. The analytical formula that allows us to calculate cross sections for any point of the parameter space can be found here [**?**], and a handful script that calculates the cross sections point by point can be found here [**?**].

In the next session we explain how we had derived results in different benchmark points, based in the above full-simulated samples.

- Distributions at Gen level

5.2.2.1 Reweighting

We are considering a $2 \rightarrow 2$ process at leading order. The two Higgs bosons are produced with identical transverse momenta (p_T^H), and they are back-to-back in azimuth at this order (before a parton shower). The final state can then be completely defined by three kinematic variables, if we ignore the irrelevant azimuthal angle of emission of the bosons. Furthermore, one of the three remaining variables can be used to isolate all the information related to the PDF of the colliding partons, which is also irrelevant to the physics of the production process once one focuses on a specific initial state (the gluon-gluon fusion process). The variable factorizing out the PDF modeling can

Node	κ_λ	κ_t	c_2	c_g	c_{2g}
1	1.0	1.0	0.0	0.0	0.0
2	7.5	2.5	-0.5	0.0	0.0
3	15.0	1.5	-3.0	-0.0816	0.3010
4	5.0	2.25	3.0	0.0	0.0
5	10.0	1.5	-1.0	-0.0956	0.1240
6	1.0	0.5	4.0	-1.0	-0.3780
7	2.4	1.25	2.0	-0.2560	-0.1480
8	7.5	2.0	0.5	0.0	0.0
9	10.0	2.25	2.0	-0.2130	-0.0893
10	15.0	0.5	1.0	-0.0743	-0.0668
11	-15.0	2.0	6.0	-0.1680	-0.5180
12	2.4	2.25	2.0	-0.0616	-0.1200
13	-15.0	1.25	6.0	-0.0467	-0.5150

Table 5.1: Parameter values of the final benchmarks selected with $N_{clus} = 13$. The first cluster is the one that contains the SM sample.

be taken as the magnitude of the boost of the centre of mass frame as seen in the laboratory frame.

The two remaining variables, which provide direct information on the physics of GF HH production, can be chosen to be the invariant mass of the HH system (m_{HH}) and the modulus of the cosine of the polar angle of one Higgs boson with respect to the beam axis ($|cos\theta^*|$). Since we are using parton-level information, this last variable is equivalent to the polar angle in the Collins-Soper frame ($|cos\theta^*_{CS}|$) [?], which is commonly used in experimental analysis. The variables m_{HH} and $|cos\theta^*|$ can thus be used to fully characterize the final state kinematics produced by different choices of the value of anomalous Higgs boson (self-) coupling parameters.

By construction the full-simulated samples listed in Tab. 5.2 are good representatives of the kinematic space. Therefore, based in the generation level m_{HH} and $|cos\theta^*|$, those can be used to construct samples to any other parameter space point.

The procedure is made as follows:

- For each new parameter space point we perform a simulation in `MG5_aMC@NLO`, asking for N events;
- We construct two dimensional histograms in the generation level m_{HH} and $cos\theta^*$, with 20 GeV-wide bins in the m_{HH} and 0.2-wide bins in $cos\theta^*$ (without the moduli);
- We construct the same histogram with the sum of all the full simulated samples described in the last section (signal dataset);

- The new sample is constructed by weigthing the signal dataset event-by-event by:
$$W_e = \frac{New_{ij}}{D_{ij}}\,, \tag{5.2}$$
where (ij) specify the bin in which the event e belongs and New_{ij} (D_{ij}) the number of events of the new signal sample (signal dataset) in that bin.

We make reweighted samples for three types of theory scans:

- A plain scan in κ_λ, while all the other parameters are kept as in SM (κ_t, $c_2 = c_g = c_{2g} = 0$), where the gen-level histograms are made from 50,000 events
- Another set of samples that we will use to calculate the shape systematics necessary to extrapolate the limits in the benchmarks to an extended part of the parameter space (see Sec. **??**).

Benchmark	κ_λ	κ_t	c_2	c_g	c_{2g}
1	7.5	1.0	-1.0	0.0	0.0
2	1.0	1.0	0.5	-0.8	0.6
3	1.0	1.0	-1.5	0.0	-0.8
4	-3.5	1.5	-3.0	0.0	0.0
5	1.0	1.0	0.0	0.8	-1
6	2.4	1.0	0.0	0.2	-0.2
7	5.0	1.0	0.0	0.2	-0.2
8	15.0	1.0	0.0	-1	1
9	1.0	1.0	1.0	-0.6	0.6
10	10.0	1.5	-1.0	0.0	0.0
11	2.4	1.0	0.0	1	-1
12	15.0	1.0	1.0	0.0	0.0
SM	1.0	1.0	0.0	0.0	0.0

Table 5.2: Parameter values of the twelve benchmarks and the Standard Model point.

5.2.2.2 Non-resonant Vector Boson Fusion

For the 2016 version of the analysis, one non-resonant VBF sample was also produced centrally with the Standard Model coupling parameters. The MiniAOD version of this sample can be found on DAS under: /VBFHHTo2B2G_CV_1_C2V_1_C3_1_13TeV-madgraph/RunIISummer16MiniAODv2-PUMoriond17_80X_mcRun2_asymptotic_2016_TrancheIV_v6-v1/MINIAODSIM

5.2.3 Background MC

Even though the signal extraction and background modeling of this analysis are performed based on data, background Monte Carlo samples are used to validate the simulation of our signal description and to develop the analysis. The main backgrounds for the $b\bar{b}\gamma\gamma$ final state come from either well-isolated photons coming from the hard scatter (prompt photons) or isolated photons reconstructed due to very collimated $\pi^0 \to \gamma\gamma$ decays fragmented from jets (fake photons). These backgrounds are the same as the ones to the SM H $\to \gamma\gamma$ analysis, and a more complete description of the samples used can be found in the H $\to \gamma\gamma$ AN [**?**, **?**].

We can classify these backgrounds with respect to the number of prompt and fake photons in the selected diphoton candidate. The prompt-prompt background events are simulated with the Sherpa generator; it includes the born processes with up to 3 additional jets at LO accuracy as well as the box processes at LO. The prompt-fake and the fake-fake contributions are simulated with PYTHIA8, with a "Double-EM Enriched" filter[4] applied during production to improve the samples selection efficiencies. Additionally, a sample of Drell-Yan events decaying into electrons, simulated at NLO with AMC@NLO, is used, although its final contribution to the event yield is minimal due to the $M(\gamma\gamma) > 100\,\mathrm{GeV}$ selection cut.

5.2.4 Data

The data samples used in this analysis correspond to approximately 36.5 fb^{-1} of data collected in 2016, reconstructed with the 80X CMSSW release.

5.3 Analysis objects and selection

This analysis uses general purpose reconstruction of the photons and jets for which we have brief descriptions below.

5.3.1 Triggers And Pre-Selection

Exploiting the high online performance of the CMS ECAL to reconstruct photons and electrons, the dataset used in this analysis is constructed with a selection that requires two photons at High Level Trigger (HLT) level.

[4] it requires a high p_{T} and well isolated photon-like signal (electromagnetic activity) coming from photons, electrons, or neutral hadrons)

For the 2016 data taking period, the online strategy was based on a single HLT trigger path:

- HLT_Diphoton30_18_R9Id_OR_IsoCaloId_AND_HE_R9Id_Mass90;

In order to achieve a good data/simulation comparison, a pre-selection that is tighter than the online selection is applied on data and Monte Carlo. This pre-selection is described on table 5.3. It is based on shower shape variables ($R9$, the ratio between the energy deposited on a 3x3 ECAL crystal matrix around the most energetic crystal in the supercluster, and the supercluster energy), isolation variables (charged hadron isolation, CHI, the sum of all charged hadron particle flow candidates energies inside a cone of $\Delta R < 0.3$ around the photon axis), identification variables (H/E, the ratio between the photon's energy deposit on HCAL and on ECAL), and kinematic variables (E_T and the photon supercluster η). Only events that have at least one diphoton candidate passing the pre-selection requirements are considered in the analysis.

Requirements	Leading Photon	Subleading Photon
E_T	30 GeV	20 GeV
$\lvert\eta\rvert$	< 2.5 and outside $1.442 \lvert\eta\rvert < 1.566$	
Shower shape and Isolation	$R9 > 0.8$ or CHI < 20 or CHI/$E_T < 0.3$	
Identification	H/E < 0.08	

Table 5.3: Trigger based pre-selection applied on diphoton candidates.

The central H $\rightarrow \gamma\gamma$ analysis provides scale factors and uncertainties related to those scale factors due to this HLT selection, which we also apply in the analysis and take into account in our final list of systematics.

5.3.2 Photons

The kinematic requirements applied on the photons, after the diphoton candidates have passed through the event pre-selection (see Section 5.3.1), is analogous to the ones used in the SM H $\rightarrow \gamma\gamma$ analysis. The selection is as follows:

- Leading photon $E_T > 30$ GeV, trailing photon $E_T > 20$ GeV;
- Leading photon $E_T/M(\gamma\gamma) > 1/3$, trailing photon $E_T/M(\gamma\gamma) > 1/4$;
- $100 < M(\gamma\gamma) < 180$ GeV.

Additionally, a photon identification requirement is applied to the photons.

In the 13 TeV run of 2016 we have at least three different identification algorithms for photons:

- General purpose cut-based ID developed by the CMS EGamma group [?]. The ID makes use only of a few variables: H/E, $\sigma_{i\eta i\eta}$ and isolation. This type of ID was used in Run-I analysis.
- General purpose MVA ID developed within the EGamma group [?]. It utilizes the information from many shower shape variables at ECAL, as well as isolation information.
- MVA ID developed by the H $\rightarrow \gamma\gamma$ search group [?] (ref to be updated). It is similar to the one developed in EGamma group, but uses a slightly different set of input variables.

We have chosen to use the EGM MVA photon ID on this analysis. The WP chosen is one that provides 90% signal efficiency for the photon selection (provided centrally). The scale factors used to ensure data/MC agreement in the selection efficiency are also applied (provided centrally). Additionally, an electron veto is applied to avoid background with electrons faking photons (scale factors provided centrally also applied).

=========== OLD ===========

Currently (as of January 2016), the available samples processed by the H $\rightarrow \gamma\gamma$ group only have stored their own training of the photon MVA ID. We have chosen working points that ensure that the resonant low mass samples have a 90% efficiency both in the barrel and the endcap ECAL regions.

ECAL Region	Hgg MVA Selection
EB	0.07
EE	-0.03

Efficiencies of the leading photon to pass the ID criteria, as a function of the photon transverse energy, are shown in Figure 5.2. Only photons matched to gen-level prompt photons are used.

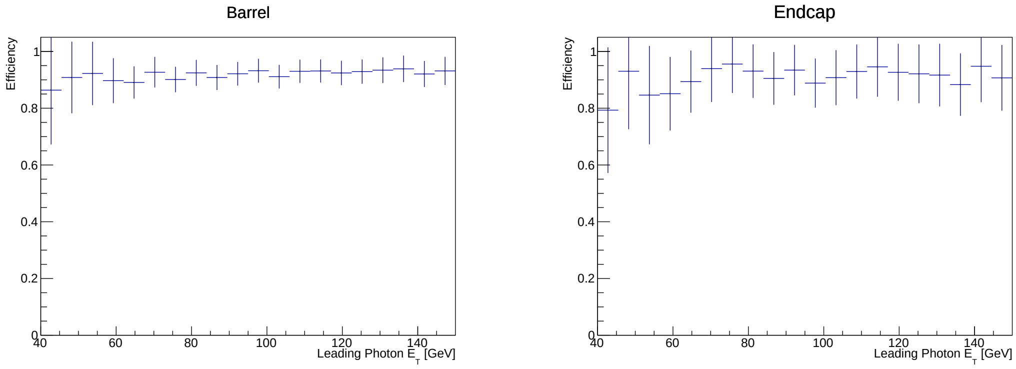

Figure 5.2: Efficiencies of the leading photon to pass the ID criteria, as a function of the photon transverse energy, for photons in the barrel and endcap regions of ECAL.

5.3.2.1 Fake Photon Control Region

A control region is created by selecting diphoton candidates with one photon that passed the ID requirement and one that didn't. All the other selections remain the same, and the procedure to select such diphoton candidate is the same as in the signal region.

This control region is used on the analysis to perform the closure test on the background modeling.

5.3.2.2 Vertex

Inheriting from the main $\mathrm{H} \to \gamma\gamma$ analysis, we use the vertex that gives the highest $\mathrm{H} \to \gamma\gamma$ vertex MVA score. Because there are additional jets in the event, picking picking this vertex has a very small mismatch efficiency. Only in less than 0.1% of the events, the chosen vertex is different from the vertex associated to the simulated event.

5.3.2.3 Gain Switch

Due to the ECAL slew rate issue discovered during the 2016 data taking, we investiaged the fraction of selected events in our blinded signal region with photons that go through gain switches. The plots on Figure 5.3 show, in bins of $\tilde{M}_X$, the fraction of events with at least one of the photon candidates going through gain switches (to gain 1, gain 6 or both). These results show that, for the high mass region, around 20% of our events are affected by gain switches. This non-negligible rate means that the analysis needs to use the re-MiniAOD Moriond17 campaign, which has the slew rate effect mitigated.

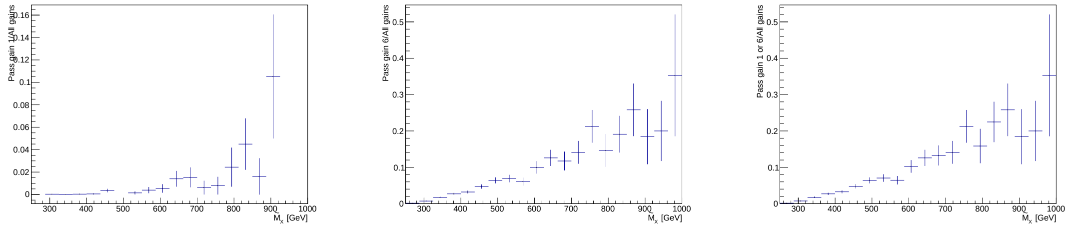

Figure 5.3: Fraction of events with photon candidates going through gain switch.

5.3.2.4 Regression

A new version of the photon energy regression has been trained (with 80X MC and 2016 data taking conditions). We compared this new regression to the previous training (74X), as seen in the plots of Figure 5.4 for three different resonance mass points. The difference observed is not large enough for this analysis to be affected, so the regression version used is 74X (following main H $\rightarrow \gamma\gamma$ analysis).

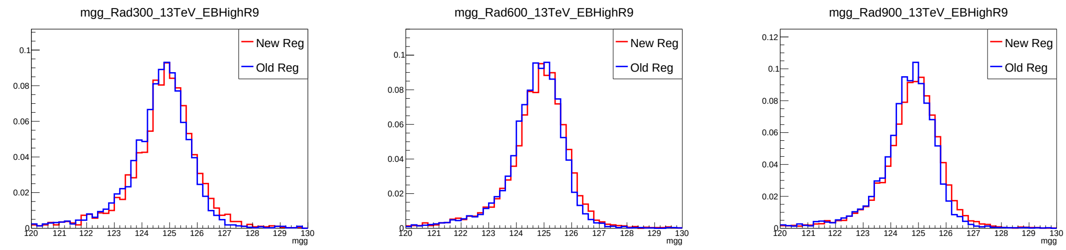

Figure 5.4: $M(\gamma\gamma)$ reconstructed with different versions of the photon energy regression.

5.3.3 Jets

Note: the jets selection has not changed with respect to the 2015 analysis.

The jets in Run-II at CMS are reconstructed using anti-kt algorithm with the distance parameter $D = 0.4$. This was a change with respect to the parameter distance of $D = 0.5$ in Run-I due to increased pile-up in Run-II data taking. This change resultes in smaller $M(jj)$ resolution but induced a bias towards lower energy of the signal $M(jj)$ peak, because less energy is clustered in a jet. This effect can be seen in figure 5.5 of the $M(jj)$ distribution for reconstructed jets matched to generator-level jets (that come from the Higgs) from the Radion sample of $M = 300\,\text{GeV}$.

We use the *Loose ID* criteria to select the jets, which is described in Ref [**?**].

The jet candidates in the event, after passing the aforementioned ID, must have $p_{\mathrm{T}} > 25\,\text{GeV}$ and $|\eta| < 2.4$ (so that they are within the tracker of CMS and can be

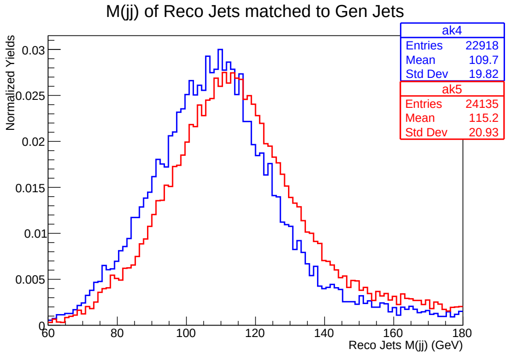

Figure 5.5: Difference between jet reconstruction used in Run I (red) and Run II (blue)

tagged as coming from b quark). The jets must also be outside the photon cone with a $\Delta R(j, \gamma) > 0.4$. Dijet objects are then created and only dijets with $M(jj)$ between 60 and 180 GeV pass the selection. If more than one dijet has passed those criteria, the dijet with two jets with highest b-tagging score (see sec. 5.3.3.2) are selected as the dijet candidate.

5.3.3.1 Jet energy regression

In addition to the misfortune of a small distance parameter of the jet reconstruction algorithm, the energy of the jets coming from b-quarks can not be fully reconstructed due to neutrinos escaping the detector. In order to improve the $M(jj)$ resolution and gain in S/B discrimination, we employ jet energy regression technique based on MC simulated samples. We use implementation of the regression in TMVA package and train it on $X \to \text{HH} \to b\bar{b}b\bar{b}$ MC samples. Input variables to the training include jet kinematics, energy deposited in the calorimeter, vertex information, and also the missing transverse energy in the event (MET). Performance of the regression was validated on MC signal samples as well as in data, based on $Z(\ell\ell) + bb$ events, where the p_T balance was checked of the $p_T(\ell\ell)$ and $p_T(bb)$. Detailed information about the training and its validation can be found in Appendix **??**.

The effect of the regression on the analysis can be summarized in figures 5.6. While data in the photon control region remains the same, the $M(jj)$ spectrum in the signal is shifted towards higher values (scale correction). This leads to an improvement in the analysis due to the gain in signal efficiency.

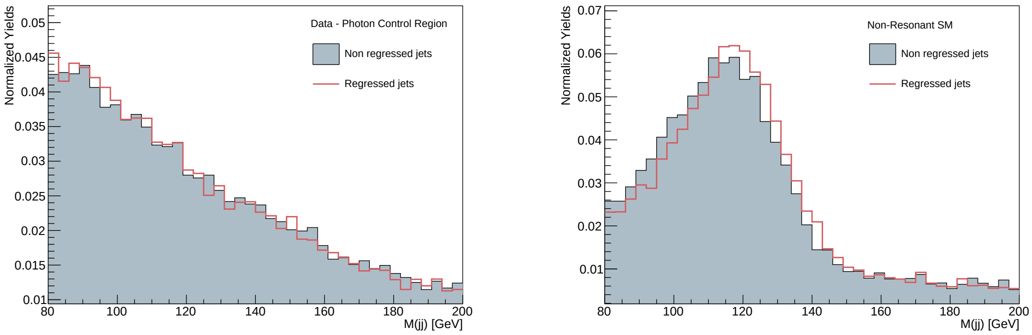

Figure 5.6: Comparison between dijet invariant mass with regressed jets and without for data in photon control region and signal MC. WARNING - THESE ARE 2015 PLOTS, NEED TO UPDATE

5.3.3.2 B-tagging

We utilize the *Combined Secondary Vertex* algorithm (CSVv2) for tagging b-jets, described in Ref. [**?**]. This b-tagging score for leading and subleading jets is then used for the resonant and non-resonant analyses categorization (see section 5.8.2).

The b-tagging scale factors have been calculated according to the BTV recipe, including the in situ calculation of signal efficiency. The signal efficiency has been calculated for all signal samples combined, in bins of p_T and $|\eta|$. The efficiency plots for tight WP, medium WP and loose WP can be seen in figure 5.7.

5.4 Categorization

To boost the sensitivity of the analysis, we divide the signal region into different categories based on the b-tagging score of the leading and subleading jets. These categories are constructed based on the most sensitive regions of the 2D plane defined by the b-tagging scores of the leading and subleading jet candidates. In order to measure the significance of these regions without using our signal region, we use the control region defined by requiring one of the photons to fail the MVA ID selection. It's important to make sure that this control region models well our signal region in our variables of interest, namely the b-tagging scores and the 4-body invariant mass. That can be infered through the plots in Figure 5.8.

By checking the ratio between the distributions of the signal region and the photon control region, before normalization, it was found that the photon control region needs to be scaled by a factor of 0.14 in order to also be consistent in terms of yields with the signal region. By the time this optimization was performed, only 22/fb of prompt

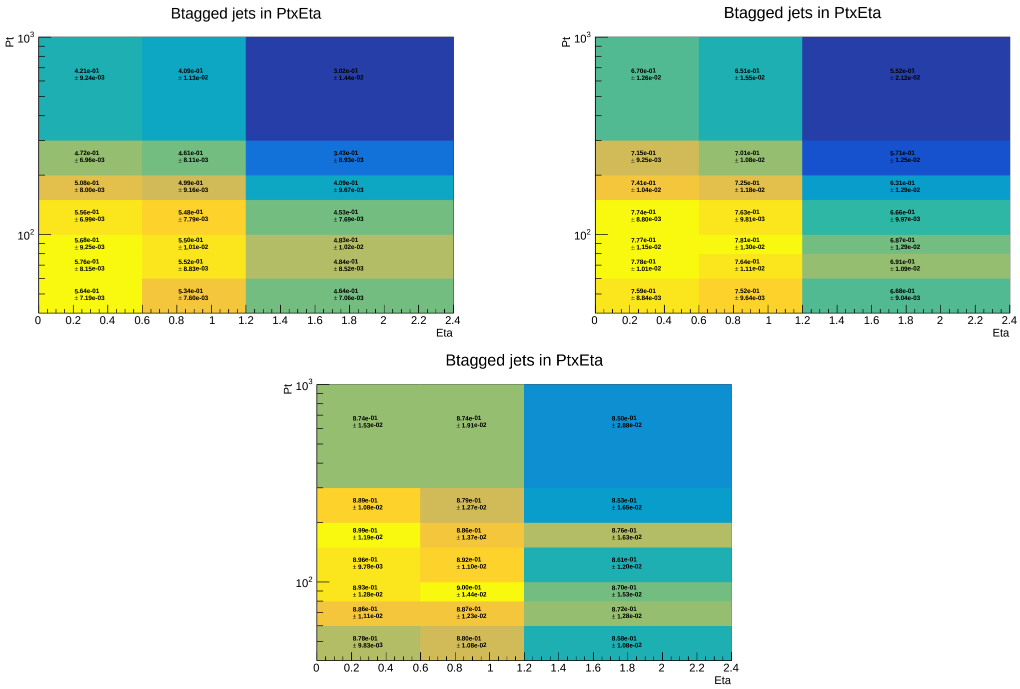

Figure 5.7: B-tagging efficiency for tight, medium and loose working points, as a function of jet p_T and $|\eta|$. WARNING - THESE ARE 2015 PLOTS, NEED TO UPDATE

reco data was available, therefore, the control region was also scaled by a factor of 35/22 in order to match the expected full integrated luminosity of 2016. For the significance calculation, we assume the SM HH signal with a cross section of 1 fb and an integrated luminosity of 35/fb. We then calculate the significance of each exclusive b-tagging bin in the b-tagging 2D plane, as shown in Figure 5.9.

With that in mind, we construct different options for the categorization schemes. These can be seen in Figure 5.10. The green squares represent the High Purity Category (HPC), the yellow squares represent the Medium Purity Category (MPC) and the blue squares represent the Jet Control Region (JCR).

Another point that needs to be checked during the categorization is the expected number of background events. Since our background estimation is data driven, with the sidebands of the diphoton and dijet mass distributions, we need to make sure some events are left to fit. Therefore, we apply the mass window requirement (for the resonant case) and the $\tilde{M}_X$ categorization (for the non-resonant case) and check the amount of expected background events. For the non-resonant case, we found that even using the most strict categorization definitions, we would still have enough expected background events for a robust description. For the resonant case, we test

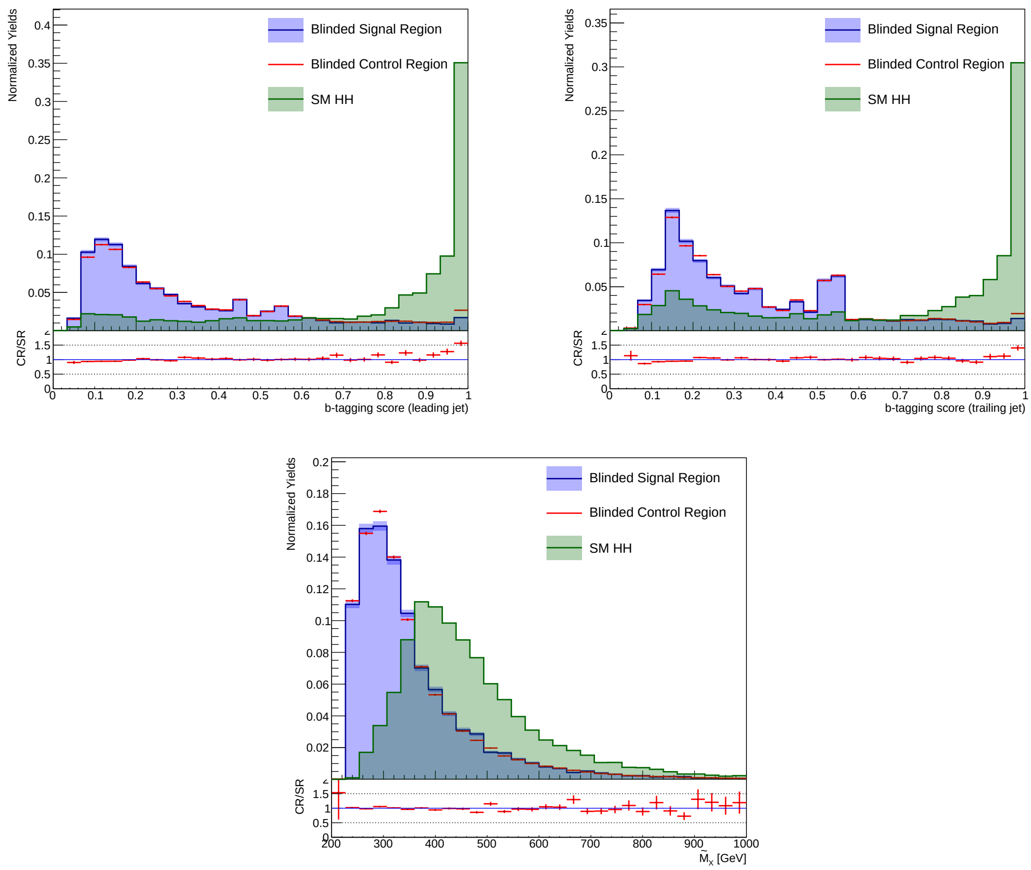

Figure 5.8: Comparison between blinded signal region and blinded photon control region in the leading jet b-tagging, subleading jet b-tagging and effective mass.

the different categorization schemes showin in Figure 5.10 to see the expected number of background events (with the photon control region) on both HPC and MPC. These mass scans can be seen in Figure 5.11.

From Figure 5.11, we see that the non-resonant proposed categorization is too tight for most of the resonance masses in both categories. Option 2 seems to give a reasonable amount of background events for the modeling up until the boundary used in 2015 to define the low/high resonant regions. Therefore, for the low mass resonant analysis ($\tilde{M}_X < 500$ GeV), we use the categorization under Option 2 in the diagrams of Figure 5.10. For the High mass resonant analysis ($\tilde{M}_X > 500$ GeV), we use the same categorization scheme that was used for the 2015 low mass resonant analysis.

In addition to the categories mentioned above, cuts on the helicity angle $|cos(\theta^*_{CS})|$ have been investigated. It was found that the cut that maximizes the sensitivity of the analysis is at 0.80 for the non-resonant categories. No cut is imposed in the resonant analysis.

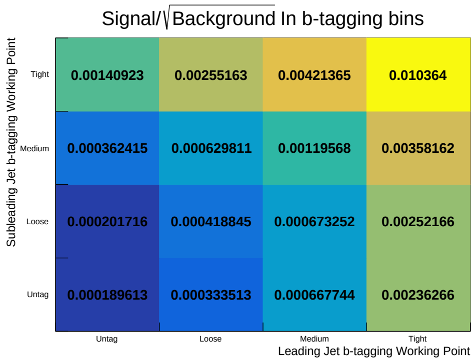

Figure 5.9: Sigificance in exclusive b-tagging bins in the 2D plane defined by the b-tagging score of the selected leading and subleading jet candidates.

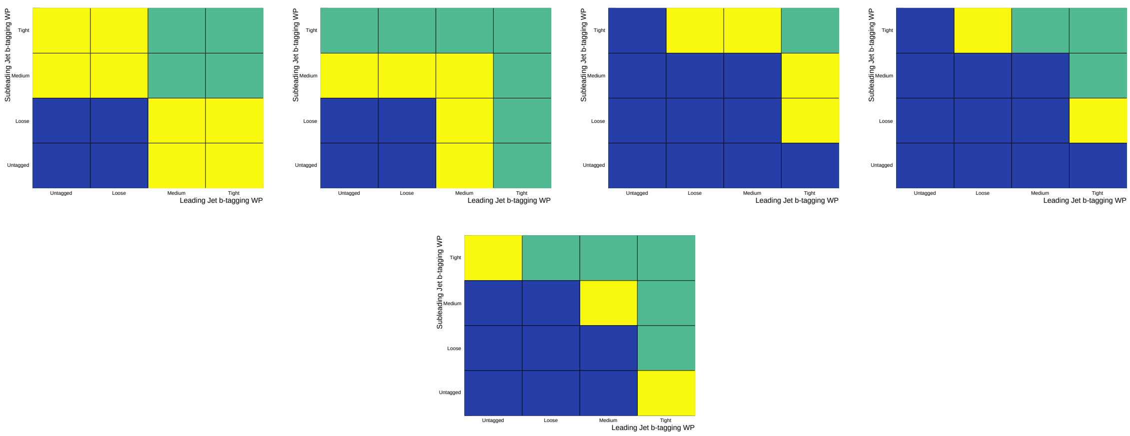

Figure 5.10: Different categorization strategies, from left to right, Run 1 categorization, 2015 low mass resonant categorization, Non-resonant option, Option 2 and Option 3.

5.4.1 MVA Categorization

During the analysis, it has been noticed that different kinematic variables could potentially contribute to tightening the signal region without cutting too much on the signal efficiency. However, this large-dimensional optimization procedure (all investigated variables) was not optimal. Instead, we have developed a multivariate analysis (MVA), combining these different variables, into a single discriminant. This discriminant is used to categorize the events in High Purity, Medium Purity categories and a control region, similarly to the cut based categorization.

The input variables investigated for this MVA were:

- Leading and subleading jets b-tagging score;

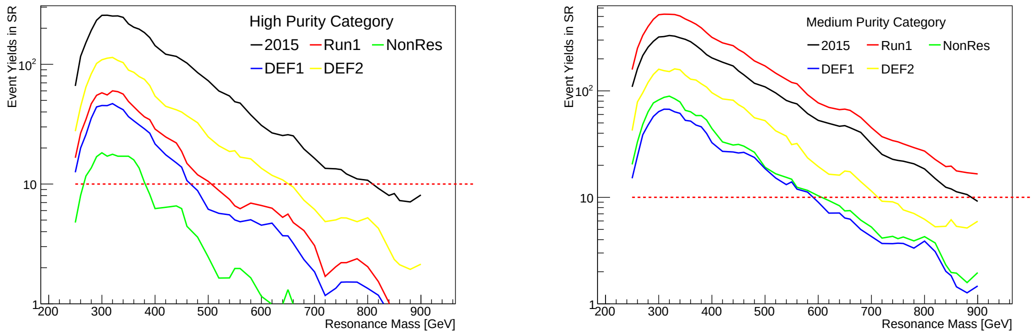

Figure 5.11: Expected background yields, from the photon control region scaled to the signal region, for the different resonant mass points (including mass window requirement), for the HPC and the MPC, respectively. Please note that "DEF1" in the legend corresponds to Option 2 in the diagrams of Figure 5.10, while "DEF2" corresponds to Option 3.

- Helicity angles $|cos(\theta^*_{CS})|$, $|cos(\theta^*_{bb})|$ and $|cos(\theta^*_{\gamma\gamma})|$: $|cos(\theta^*_{CS})|$ is defined as the angle between the direction of the $H \to \gamma\gamma$ candidate to the Colin-Sopper reference frame (assumes each incoming particle in the scattering to have 6.5 TeV); $|cos(\theta^*_{xx})|$ is defined as the angle between the particle x and the direction defined by the $H \to xx$ candidate (randomly choosing between x's), where $x = \gamma$ or b;

- $p_T(\gamma\gamma)/M(jj\gamma\gamma)$ and $p_T(jj)/M(jj\gamma\gamma)$

The training was performed in the photon control region, as described in 5.3.2.1, modeling our background. Plots comparing the input variables in the photon control region and the blinded signal region are shown in Figure 5.12. As our signal in the training, we sum the 14 non-resonant HH samples available (box only, SM, and 12 BSM points). Thus, we have a training that is not specific to a single region in the parameter space, maintaining the sensitivities comparable between the benchmark points (as it is with the cut based categorization).

To improve the training, we split the training into two regions: Low Mass and High Mass. The low mass training is performed with events with $\tilde{M}_X$ below 400 GeV, while the high mass training uses the complementary region. The training is based on a decision tree boosted with the gradient algorithm, with the trees randomized between iterations to decrease overtraining. To implement the training the TMVA package was used. The TMVA output plots are shown for both trainings in Figures 5.13 and 5.14. From now on, we will refer to the trainings discriminant variable as HHTagger.

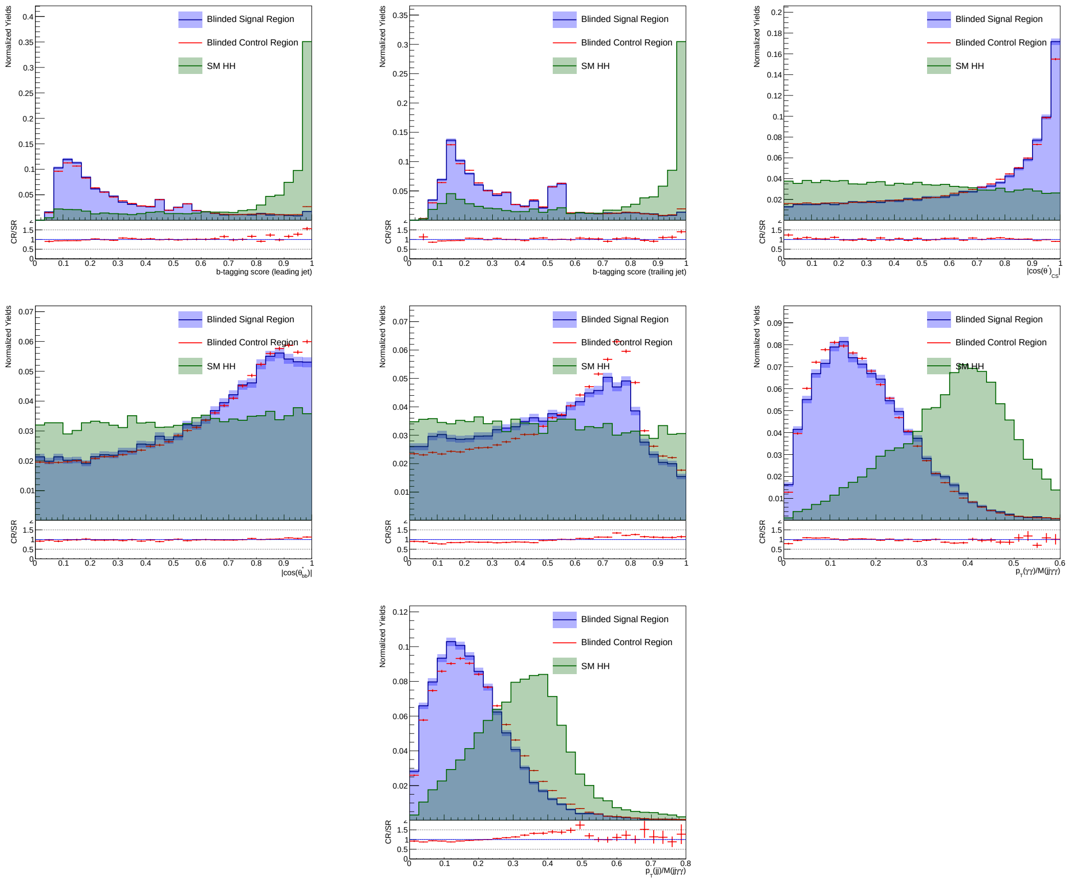

Figure 5.12: Distributions of input variables in the blinded photon control region, blinded signal region, and SM HH sample. All normalized to unity.

With the HHTagger discriminant, we build our two signal categories based on the maximal S/sqrt(B) point, separately in the high mass and in the low mass regions. As signal, we use the SM HH sample to calculate the sensitivity. The outcome of this study was the categorization in table 5.4. The expected number of background events, when comparing MPC and HPC between cut based and MVA approaches, is comparable and consistent, while for the number of signal events, the performance is better for the HHTagger categorization.

We have also to insure that the HHTagger selection does not shape our variables of interest, $M(jj)$ and $M(\gamma\gamma)$. We demonstrate that there is no appreciable shaping by comparing the $M(jj)$ and $M(\gamma\gamma)$ shapes in different bins of the HHTagger discriminant. This can be seen in Figure 5.15.

Mass Region	HPC	MPC
Low Mass	HHTagger > 0.96	$0.75 <$ HHTagger < 0.96
High Mass	HHTagger > 0.96	$0.6 <$ HHTagger < 0.96

Table 5.4: Non-resonant categorization with HHTagger discriminant.

5.4.1.1 Performance Cross-Checks

We have performed several cross checks to look for possible improvements on the categorization MVA.

- **Signal Hypothesis**

In the standard training, the sum of all non-resonant samples are used as signal hypothesis. However, this might not be the optimal training for the SM HH case. To test this, we compare the performance of different trainings assuming the SM HH signal. The signal hypotheses tested are:

- All non-resonant (standard);
- SM HH;
- SM HH, with separate training for the high mass and low mass region (similar to standard);
- SM HH + Benchmark 3 (this benchmark point refers to the node that contains the SM point);
- SM HH + Benchmark 3, with separate training for the high mass and low mass region (similar to standard).

The background hypothesis for this test is the photon control region, in the high mass region.

The ROC curves from the different trainings are shown in Figure 5.16. Since no significant improvement is seen in the high purity region (for background rejection larger than 95%, a typical value for the chosen WPs), the standard training method is kept in use.

- **Background Hypothesis**

In the standard training, the photon control region is used as a background model, avoiding MC reliance. However, this might not be the optimal because the photon control region might have different correlation between the MVA variables with respect to the signal region. To test this, we compare the performance of different trainings assuming different background hypotheses:

- Photon control region (standard);
- Blinded signal region;
- Blinded control region (to insure that the difference between the two previous trainings does not come from blinding).

The background hypothesis for this test is the blinded signal region, in the high mass region, and the signal hypothesis is SM HH.

The ROC curves from the different trainings are shown in Figure 5.17. While some improvement is seen, this training is not optimal for statistical reasons. The blinded signal region contains significantly less events than the photon control region. This limits the precision and accuracy of the multivariate analysis training. Specifically, it has been observed that the blinded signal region does not contain events in the high BDT region (signal-like phase space), which can cause over training. The second issue is that, optimally, training on a dataset that is statistically independent from the one to which it will be applied leads to a more robust procedure.

- **Resonant Hypothesis**

While this MVA is trained with the non-resonant signal hypotheses, it can also be applied to the resonant search. We check, however, if a dedicated training with the resonant samples as signal hypothesis performs better, when applying the categorization to the resonant analysis. This is tested by comparing the categorization performance of the standard training versus a resonant training on a resonant signal point. The plot in Figure 5.18, these two trainings are shown and no significant difference is seen. Therefore the standard, non-resonant training will be used also for the resonant analysis.

5.5 $\tilde{M}_{\mathrm{X}}$ and Mass Window Selection

In order to increase the sensitivity of the resonant analysis, we perform a cut on the 4-body invariant mass before the signal extraction with the 2D fit. In the Run I analysis, the 4-body invariant mass was corrected with a kinematic fit, to mitigate the effects of the low mass resolution of the dijet system. However, it has been seen that this method is too reliant on the a-priori set of energy and spatial resolutions for the jets in that analysis (these resolutions must be measured in situ, since they are kinematic dependent). One solution for this was to use instead the variable $\tilde{M}_{\mathrm{X}}$, defined as:

$$\tilde{M}_{\mathrm{X}} = M(jj\gamma\gamma) - M(jj) - M(\gamma\gamma) + 250 \text{ GeV}. \tag{5.3}$$

This variable performs a kinematic fit "by hand", by effectively scaling the dijet and diphoton invariant masses to 125 GeV. In order to quantify the improvementof this variable with respect to other 4-body invariant mass reconstructions, we calculate the width of the smallest interval that covers 68% of the signal shape in each reconstruction method. We compare $\tilde{M}_{\mathrm{X}}$ with the standard $M(jj\gamma\gamma)$ and with $M(jj\gamma\gamma)_{KF}$, which is reconstructed with a kinematic fit in $M(jj)$, which tries to vary the jets within their uncertainties to achieve $M(jj) = 125$ GeV. The widths are compared in Figure 5.19.

The effect of reconstructing the 4-body invariant mass with $\tilde{M}_{\mathrm{X}}$ on the signal shape can be seen in 5.20. The figure shows that the $\tilde{M}_{\mathrm{X}}$ reconstruction yields a better performing resolution for the 4-body invariant mass reconstruction, meaning that we can perform tighter cuts on it and increase the signal/background for each signal mass point.

One extra check we must do while using this variable is to make sure there are no unexpected effects on the background shapes. The effect of $\tilde{M}_{\mathrm{X}}$ is similar to the kinematic fitted $M(jj\gamma\gamma)$, but more pronounced, which is the sharp kinematic cut around the $\tilde{M}_{\mathrm{X}} = 250$ GeV point. This can be seen in the figures in section 5.7..

It has also been observed that, for the non-resonant signal samples, the $\tilde{M}_{\mathrm{X}}$ variable approaches the generator level HH invariant mass distribution more so than the kinematic fitted $M(jj\gamma\gamma)$ and the default 4-body invariant mass. This can be seen in figure 5.21. For this, $\tilde{M}_{\mathrm{X}}$ will also be used in the non-resonant analysis.

One desirable effect of the $\tilde{M}_{\mathrm{X}}$ definition in this version of the analysis, compared to the 2015 definition (which only scaled the $M(jj)$ value as in $\tilde{M}_{\mathrm{X}} = M(jj\gamma\gamma) -$

$M(jj) + 125$ GeV), is that a $\tilde{M}_{\mathrm{X}}$ selection does not bias $M(\gamma\gamma)$ and $M(jj)$. This can be seen in the 2D plots of $\tilde{M}_{\mathrm{X}} : M(\gamma\gamma)$ and $\tilde{M}_{\mathrm{X}} : M(jj)$ in Figure **??**.

With $\tilde{M}_{\mathrm{X}}$, we can improve the resonant analysis by tightening the signal region around the 4-body resonance mass (mass window). Through limits optimization, it has been checked that constructing a mass window with the smallest interval that covers 60% of the signal shape provides the best sensitivity. The size of these intervals, as a function of the hypothesis mass, is seen in Figure 5.23.

We implement this mass window by requiring that $W_{-} < \tilde{M}_{\mathrm{X}} < W_{+}$. $W_{\pm}$ are calculated based on the widths defined in Figure 5.23. We fit $W_{\pm}$ with a 3rd degree polynomial so that the mass windows can be defined functionally based on the mass hypothesis. These fits, and, therefore, the definition of $W_{\pm}$ can be seen in Figure 5.24. $W_{\pm}$ can be infered through the Y-axis of 5.24, W_{-} is defined by the blue curve and W_{+} by the red.

5.6 Selection Efficiencies

As a summary of the previous sections, the cut flow of the analysis is as follows:

- At least two photons and two jets in the event
- At least two photons pass the trigger based pre-selection (see sec. 5.3.1);
- At least two photons pass the kinematic and identification requirements (see sec. 5.3.2) $\rightarrow$ select two highest E_T photons as diphoton candidate;
- At least two jets pass the kinematic selection (see sec. 5.3.3) $\rightarrow$ select two jets with highest b-tagging score as dijet candidate;
- Event can be classified in either High Purity Category or Medium Purity Category;

The efficiency after each step above and taking into account the acceptance is estimated and shown for each of the signal samples considered in our analysis. Figure 5.25 shows the cut flow efficiency$\times$acceptance for the graviton signal samples ranging from mass hypothesis of 250 up to 900 GeV on the top left. It shows the one with the bjet regression applied, on the top right and the ratio of the efficiencies of the two on the bottom. figure 5.26 shows the analog cut flow efficiency$\times$acceptance of the Radion samples (with mass range of 250 to 900 GeV) on the top left. It shows the same cutflow with the bjet regression applied, on the top right and the ratio of the efficiencies of the two on the the bottom. Figure 5.27 and figure 5.28 show the analog cutflow×acceptance of the 14 nodes of nonresonant signal benchmarks corresponding to 12 anomalous couplings combinations, in addition to the box diagram(node=0) and the SM couplings (node=1) as defined in subsection 5.2.2 and in table 5.2. Figure 5.27 displays the values for the cut based categorization on the top left, the ones with the MVA based categorization on the top right and the ratios of the two on the bottom. Figure 5.28 shows the values when the b-jet regression is applied in addition the MVA based categorization in the left, and the ratio of the two.

These figures report results using for the above described selections where the photon identification is the H $\rightarrow \gamma\gamma$ MVA procedure.

5.7 Control Plots

In order to validate the Monte Carlo simulations, we produce data/Monte Carlo comparison plots (control plots) of the light jets control region (JCR, 0 medium b-tagged jets) and of the signal region (SR), both blinded in the $115 < M(\gamma\gamma) < 130$ GeV region. In order for background and data to match, the DiPhoton+Jets contribution has been scaled by a factor of 1.5, while the prompt-fake and fake-fake contributions from the GJets and QCD samples have been scaled to data. It should be stated that the background MC is not used at any time in this analysis. The signal in these plots is normalized for 500 fb.

5.8 Statistical Modeling and Limit Extraction

The signal extraction and limit setting in this analysis is performed with a 2D fit on the $M(\gamma\gamma) : M(jj)$ plane, since we expect our signal to peak in both axes. For our background, they are expected to be uncorrelated given our statistical precision. With this last assumption, we can construct background function models as $f_\gamma(M(\gamma\gamma)) \times f_J(M(jj))$, where f_γ (f_J) are our functional choices to fit the diphoton (dijet) mass spectrum. A thorough explanation of the background uncorrelation hypothesis is given at the end of this section.

5.8.1 Signal Model

As a signal model in the limit extraction, we use parametric models fitted to the simulated samples after the full selection. Each fit is done in each different sample independently, i.e., for all resonance masses, spins and for all different non-resonant hypotheses. The choice of parametric model for $M(\gamma\gamma)$ and $M(jj)$ individually is a double sided Crystal-Ball function. The double sided Crystal-Ball function is defined as follows:

$$f(x;\mu,\sigma,\alpha_L,p_L,\alpha_R,p_R) = N\cdot\begin{cases} A_L\cdot\left(B_L-\frac{x-\mu}{\sigma}\right)^{-p_L}, & \text{for } \frac{x-\mu}{\sigma} > -\alpha_L \\ A_R\cdot\left(B_R+\frac{x-\mu}{\sigma}\right)^{-p_R}, & \text{for } \frac{x-\mu}{\sigma} > \alpha_R \\ e^{\frac{(x-\mu)^2}{\sigma^2}}, & \text{for } \frac{x-\mu}{\sigma} < -\alpha_L \text{ and } \frac{x-\mu}{\sigma} > \alpha_R \end{cases}, \tag{5.4}$$

where the A_L, A_R, B_L, B_R constants are defined by:

$$A_k = \left(\frac{p_k}{|\alpha_k|}\right)^{p_k}\cdot e^{-\frac{\alpha^2}{2}}, \tag{5.5}$$

$$B_k = \frac{p_k}{|\alpha_k|} - |\alpha_k|, \tag{5.6}$$

where k is either L or R. This definition is such that there are two independent tails, a left tail (L) and a right tail (R), and a gaussian core. This signal model is enough to model both the high mass resolution of $M(\gamma\gamma)$ and the lower resolution of $M(jj)$. With respect to the signal model chosen for previous versions of the analysis, such as the 2015 analysis, this choice is beneficial when comparing to a sum of a gaussian and a single sided Crystal-Ball because the left and right tails are made completely independent, while maintaining the same number of free parameters.

These signal fits can be seen in figures **??**, **??**, **??**, **??** and **??** for the250, 300, 400, 600 and 900 GeV Radion signals, and in figures 5.42 and **??** the signal fits for the non-resonant SM HH production in the high mass and low mass categories, respectively.

5.8.1.1 Correlation Studies

The choice of parametric signal model makes the assumption that the full 2D distribution can be modeled by a product of PDFs. This choice is not the most general one, as it does not model correlations between $M(jj)$ and $M(\gamma\gamma)$. One important question, therefore, is whether the analysis is sensitive to correlations that are not modeled by our choice of signal model. To study this, we study the differences between the MC signal simulation and the 2D fitted PDF via residues:

$$R_{ij} = \frac{N_{ij}^{\mathrm{PDF}} - N_{ij}^{\mathrm{MC}}}{\sigma_{N_{ij}^{\mathrm{PDF}}}^{\mathrm{Poisson}}}, \tag{5.7}$$

where ij refers to bin i in $M(\gamma\gamma)$ and bin j in $M(jj)$, and $\sigma_{N_{ij}^{\mathrm{PDF}}}^{\mathrm{Poisson}}$ is the Poissonian error of the expected (PDF) and observed (MC). These residuals are shown in Figures

5.43, 5.44, 5.45 and 5.46. The signal MC normalization for these plots are to 1/fb signal cross section. We see no structures in the residual plots in the region where the signal is expected, therefore, we assume that the PDF product modeling is good enough given the statistical precision we have.

5.8.2 Background Model

To study the background fits, we use the fake photon control region (one photon in the diphoton candidate fails the identification requirements). From this control region, we randomly pick the number of events that is expected from the signal region under study according to the reweighted control sample described in section .

The functional choice to model the background in both fitting variables is the Bernstein family of polynomials. We also assume that the same order of polynomial is to be used in both variables. This comes from the fact that the order of the polynomial is related to the precision of the fit (degrees of freedom), which, in turn, is related to the number of events being fitted.

The first study performed is the order fixing. We fit consecutive orders of the three families of functions and check the $2\Delta NLL$ between the two consecutive fits. This $2\Delta NLL$ should be distributed as a $\chi^2(\alpha)$ distribution with the number of degrees of freedom equal to the difference in number of free parameters between the two consecutive orders (α). We then calculate the p-value of having a $2\Delta NLL$ higher than the one calculated before, given the $\chi^2(\alpha)$ distribution. If this p-value is lower than 0.05, we accept the higher order function, and continue the procedure for the next order. If this p-value is higher than 0.05, the higher order function is assumed to be too flexible given the data and the procedure terminates having found the highest order suitable function.

Due to the different regimes of our signal regions after the mass window requirements and of the non-resonant selection, it is expected that our fits will involve very different background yields. For that, we perform the $2\Delta NLL$ test in all different signal regions. The result of this test are regions of validity in number of background events to be fit. This means that the choice of Bernstein order will depend on the number of events being fitted in a given signal region. The results of the study show that, for fits with less than 15 events, a 1st Order Benstein passes the $2\Delta NLL$ test. For fits with 25 or more events, but less than 200, a 2nd Order Bernstein passes the $2\Delta NLL$ test. For fits with 200 or more events, a 3rd Order Bernstein passes the $2\Delta NLL$ test.

5.8.2.1 Bias Studies

After the order fixing, we must ensure that the functional form chosen does not bias a possible signal strength measurement in the analysis. This can happen because the real background shape that is being fitted might not be exactly the chosen functional form. Since we have no way of defining what this true shape is, we compare the signal strength measured (μ) from the background models with respect to different background shape hypotheses, as produced by toy Monte Carlo.

The goal is to find at least one background model that can fit other background shapes without a statistically significant bias in the signal strength reconstruction. The goal of having a background model with a bias less than 0.14 for all assumed shapes is set. This is justified by investigating the effect that a signal strength bias can be correct by increasing the uncertainty on μ until the true value is within the 1σ coverage of μ CITE JOSH.

We compare our 2D Bernstein model to models constructed with a Laurent series for both $M(\gamma\gamma)$ and $M(jj)$, and with sums of exponentials for both $M(\gamma\gamma)$ and $M(jj)$. We construct models with different Laurent and Exponential sum orders.

The first step in the bias studies is to get pre-fit shapes of all background models. This is done in the same datasets used for the order fixing procedure: fake photon control region scaled to match the statistics found in different data signal regions.

After the pre-fit shapes are constructed, toy Monte Carlo events are generated based on the pre-fitted background models. Batches of 2000 toy datasets are thrown for each background model. These toys are thrown injecting also signal events, according to the signal yields expected in each category. For that, we assume a signal cross section of 1 fb, for all resonant mass points and non-resonant benchmark points. Finally, the third step is fitting the 9 batches of toy datasets with the same background models and extracting the μ from each of the 2000 toy datasets. Both the toy generation and the fitting steps are done with the CMS combine tool CITE COMBINE.

5.8.2.2 Goodness of Fit

To check how well the background model fits the data, we perform a goodness of fit test in our blinded signal region. The Kolmogorov-Smirnov (KS) test was chosen for its good performance on unbinned datasets, which is the case of this analysis. Unfortunately, no 2-dimension unbinned KS tests are available with the current tools used in CMS. The procedure taken was, then, to bin the 2D distribution with the analysis binning (40 bins in $M(jj)$ and 60 bins in $M(\gamma\gamma)$), making sure that the number of bins is much larger than the expected number of events (2400 bins is the case). For the blinding procedure, we set the bins of the 2D histograms to 0 in the blinding region ($120 < M(\gamma\gamma) < 130$ GeV). The requirement of the KS goodness of fit test is that the KS probability is ¿¿ 0.05, which is achieved for all the categories and signal regions (all KS probabilities larger than 0.45).

5.8.2.3 Correlation Studies

Assuming that the overall 2D shape can be modeled by a 2D second order polynomial, the most general function can be constructed as:

$$f(x,y) = \sum_{i=0}^{i=2}\sum_{k=0}^{k=2} c_{ik}x^i y^k, \tag{5.8}$$

where, in our case, $x = M(\gamma\gamma)$ and $y = M(jj)$ or vice-versa. However, in our modeling, we assume $M(\gamma\gamma)$ and $M(jj)$ to be independent, therefore, our choice of model takes the form of:

$$g(x,y) = \left(\sum_{i=0}^{i=2} a_i x^i\right)\left(\sum_{k=0}^{k=2} a_k y^k\right). \tag{5.9}$$

While the first equation has 9 degrees of freedom, the second only has 6. Therefore, by assuming our two parameters of interest to be independent, we lose three degrees of freedom in our model PDF. To study our sensitivity to these missing degrees of freedom, we construct a new PDF adding back three new parameters, namely:

$$g_{corr}(x,y) = \left(\sum_{i=0}^{i=2} a_i x^i\right)\left(\sum_{k=0}^{k=2} a_k y^k\right) + \alpha\cdot M(\gamma\gamma)\cdot M(jj) + \beta\cdot M(\gamma\gamma)^2\cdot M(jj) + \omega\cdot M(\gamma\gamma)\cdot M(jj)^2. \tag{5.10}$$

We perform two tests with this PDF:

- We generate Asimov datasets with $g_{corr}(x,y)$ for varying (α,β,ω) and then fit it with $g(x,y)$. Then we check the residuals comparing $g_{corr}(x,y)$ and $g(x,y)$ assuming different normalizations (i.e., different number of expected background events).

- We generate toy datasets with $g_{corr}(x,y)$ for varying (α,β,ω), with different values for the expected number of background events, with injected signal. Then we measure back the signal strength by using $g(x,y)$ and check the bias ($B = (\mu_{measured} - \mu_{true})/\sigma_\mu$)

In Figure 5.51, the 2D distributions of $g_{corr}(x, y)$ for different values of α, where the change in correlation between x and y can be seen. In Figure 5.52, the 2D distributions of $g(x, y)$ fitted to the Asimov datasets produced with $g_{corr}(x, y)$ with different values of α, where the change in correlation between x and y can be also be seen, albeit different from $g_{corr}(x, y)$. Therefore, we need to measure how sensitive we are to that difference. The first check is to calculate the 2D residuals, as was done for the signal correlation tests, between these two hypotheses, for different background normalizations. The residuals with the background normalized to 200 events can be seen in Figure 5.53, and for 100000 events in Figure 5.54. While very little statistically significant deviation is seen for 200 background events, structures do start to appear with 100k background events, which is an expected behavior. This test was further performed with 10, 100, 500, 1000, 5000 background events, with conclusions similar to the 200 case. The test was also performed with varying β and ω with similar conclusions.

For the second test, instead of generating Asimov datasets, we generate toy MC for the different normalizations and (α, β, ω) hypotheses. We then show the bias measurement for these different cases, in the hypothesis of varying α, in Figure 5.55. Since no bias larger than 14% is seen, we don't include any systematics on the signal strength due to possible background correlations that are not modeled by our choice od PDF.

5.8.3 Single Higgs Background Modeling

Apart from the smoothly-falling background expected, depending on the integrated luminosity with which it is performed, the non-resonant analysis is also sensitive to the SM single Higgs production background. In the resonant case, the mass window requirement reduces the single Higgs contributions to negligible levels, and therefore is not considered.

The SM single Higgs background consists on the Higgs resonance in $M(\gamma\gamma)$ and a $M(jj)$ shape that depends on the production mechanism. For single Higgs produced via gluon fusion and vector boson fusion, the two extra jets will constitute a smoothly falling background, therefore, we model this contribution in the 2D $M(\gamma\gamma) : M(jj)$ plane with a product of a double sided Crystal-Ball (similar to our signal model) and a second order Bernstein. For single Higgs produced in association with top quarks, bottom quarks and a vector boson, we are also able to model $M(jj)$ with a double sided Crystal-Ball, given the kinematic turn on present in the first two cases, and the $V \to jj$ resonance in the latter. The Higgs model fits are shown in Figures 5.56,

	Cross section (pb)	HM-HPC (%)	HM-MPC (%)	LM-HPC (%)	LM-MPC (%)
ggH	44.14	0.029 ± 0.0017	0.148 ± 0.0038	0.033 ± 0.0018	0.151 ± 0.0039
VBF	3.7820	0.038 ± 0.001	0.239 ± 0.0025	0.048 ± 0.0011	0.242 ± 0.0025
VH	2.257	0.271 ± 0.0038	0.748 ± 0.0063	0.367 ± 0.0044	0.962 ± 0.0071
$b\bar{b}$H	0.488	0.0297 ± 0.0035	0.262 ± 0.010	1.02 ± 0.020	2.59 ± 0.032
$t\bar{t}$H	0.5071	3.41 ± 0.027	3.69 ± 0.029	8.38 ± 0.042	8.17 ± 0.042

Table 5.5: Standard Model single Higgs cross sections at 13 TeV with their respective selection efficiencies for the four different non-resonant analysis categories: High Mass-High Purity, High Mass-Medium Purity, Low Mass-High Purity and Low Mass-Medium Purity categories.

5.57, 5.58, 5.59 and 5.60. The cross sections used for the SM single Higgs estimations are listed in table 5.5, along with their efficiencies in the four different non-resonant analysis categories.

5.9 Systematics

The expected number of signal events in this analysis is projected with Monte Carlo simulation. Possible differences between data reconstruction and Monte Carlo reconstruction are usually corrected with data/Monte Carlo scale factors. In this analysis, the systematics related to those differences come in two possible categories: normalization uncertanties and shape uncertainties. The normalization systematics are related to the uncertainty in the expected number of signal events. This is due to different efficiencies of the analysis selections in data and Monte Carlo reconstructions. Shape systematics are important in this analysis because the signal shapes enter the signal extraction procedure in the parametric fits. Therefore, uncertainties in the shape of $M(\gamma\gamma)$ and $M(jj)$ distributions must be included as systematics.

Both normalization and shape uncertainties come from photons and jets. Since the photons in this analysis are selected with the same selection criteria as the SM H $\rightarrow \gamma\gamma$ analysis, we take the photon related systematics from that. This includes the photon energy scale (PES) and photon energy resolution (PER). These two uncertainties are translated into two shape systematics ($\Delta M(\gamma\gamma)/M(\gamma\gamma)$ and $\Delta\sigma_{M(\gamma\gamma)}/\sigma_{M(\gamma\gamma)}$), and into the photon selection selection acceptance uncertainty (which inclues the trigger pre-selection requirements). The PES has to cover as well effects of linearity in the energy scale for high E_T. For this, $\Delta M(\gamma\gamma)/M(\gamma\gamma)$ is kept at 0.7% (cite diphoton high mass moriond PAS) for 2015 and 0.05% for 2016 (cite Hgg presentation on Higgs recap).

For jets, the jet energy scale (JES) and jet energy resolution (JER) are important ingredients in the list of systematics. As for photons, they enter in the analysis in two shape systematics ($\Delta M(jj)/M(jj)$ and $\Delta\sigma_{M(jj)}/\sigma_{M(jj)}$), and in the jet selection acceptance uncertainty (related to the jet kinematic requirements). An extra jet related systematic is related to the b-tagging requirements. The analysis has defined four b-tagging regions in total (two for resonant and two for non-resonant); for each one, the uncertainty of the b-tagging efficiency must be taken into account.

An extra set of normalization systematics are needed because of the mass window requirement in the resonant analysis. This systematic is related to the change in signal efficiency after variations of PES/PER/JES/JER.

A systematic due to the uncertainty in the integrated luminosity measurement in CMS is included.

No theory systematics are applied to our BSM signals.

The values of those quantities are shown in table 5.6 for 2015 data and will be updated with 2016 values.

Sources of Systematical Uncertainties	Type	Value
General uncertainties		
Integrated luminosity	Normalization	2.7%
Photon related uncertainties		
Photon energy scale ($\frac{\Delta M(\gamma\gamma)}{M(\gamma\gamma)}$)	Shape	1.0%
Photon energy resolution ($\frac{\Delta\sigma_{\gamma\gamma}}{\sigma_{\gamma\gamma}}$)	Shape	1.0%
Diphoton pre-selection (with trigger uncertainties)	Normalization	2.0%
Photon Identification	Normalization	1.0%
Jet related uncertainties		
Jet energy scale ($\frac{\Delta M(jj)}{M(jj)}$)	Shape	2.0%
Jet energy resolution ($\frac{\Delta\sigma_{jj}}{\sigma_{jj}}$)	Shape	8.0%
Resonant specific uncertainties		
Mass window selection (with jet selection uncertainty)	Normalization	5.0%
b tagging efficiency (Low Mass, high purity)	Normalization	2.5%
b tagging efficiency (Low Mass, medium purity)	Normalization	1.0%
b tagging efficiency (High Mass)	Normalization	1.0%
Nonresonant specific uncertainties		
Jet Selection plus $\tilde{M}_{\mathrm{X}} > 350$ GeV	Normalization	3.0%
b tagging efficiency (high purity)	Normalization	4.5%
b tagging efficiency (medium purity)	Normalization	1.0%

Table 5.6: Summary of systematic uncertainties. The uncertainty in the b tagging efficiency is anticorrelated between the b tag categories.

5.9.1 Signal shape smearings

One important ingredient when applying the analysis systematics is the smearing of the signal shapes. After the signal model is fitted to the signal simulation, all PDF parameters are fixed. Following, the signal mean and width are then multiplied by smearing factors related to scale and resolution uncertainties, respectively. While this is clearly un-problematic for the mean, since it merely causes a scaling of the x axis, this might not be the case for the resolution smearing. In the latter case, the tail parameters of the signal modeling can be affected by the smearing and not correspond to the frozen parameters from the pre-smearing fit. To test this, we fit the smeared MC (MC with photon and jet energy resolution smearing uncertainty values applied) with the signal PDF with the tails fixed to their values from the un-smeared MC (MC with central values of smearings) and we compare with the smeared MC fit with the signal PDF without fixing the tail parameters - these different fits are shown in Figures 5.61 and 5.62. We have also compared the 2D residuals (as defined in the Signal Model section) of the fixed tails PDF vs the smeared MC with the floating tails PDF vs the smeared MC, shown in Figure 5.63. Additionally, we compare the fixed and floating fit shapes in Figure 5.64. Since no issue has been seen, we continue using the procedure described in the previous section for applying the signal smearing.

5.10 Results

The limits shown in this section are obtained with the Higgs Combination tool, with the Asymptotic method. It has been noticed in the analysis that the central expected values can change by up to 15% when running the full CLs method. The full CLs method, however, takes considerably longer to run, therefore, the full CLs limits did not get ready for the freezing deadline.

Figure 5.65 shows the results on spin-0 resonances. Figure 5.66 shows the results on spin-2 resonances. Figures 5.67 (in fb) and 5.68 (normalized to SM cross section) show the SM-like non-resonant limit and its breakdown in the different analysis categories: LM (Low Mass), HM (High Mass), MPC (Medium Purity Category), and HPC (High Purity Category).

5.11 BSM Nonresonant Results

In addition to determination of the limit on the SM process, we are able to provide the results for BSM couplings as described 5.2.2. For the non-resonant signal samples corresponding to combinations of five anomalous couplings (κ_λ. κ_t, c_2, c_{2g}, and c_g) listed in Table 5.1 (these are also called "nodes"), the limits are shown on Fig. 5.69. The limits for the benchmarks listed in Table 5.2 and described in Sec. 5.2.2 are shown in Fig. 5.70. Figure 5.71 shows the "lambda-scan" - the upper limits for the assumption of changing κ_λ, while keeping other couplings fixed to their SM values. Figure 5.72 shows a scan over $\lambda - \kappa_t$ parameter space (this plot is for ICHEP dataset, NEEDS to be updated for 2016 data).

5.12 Summary

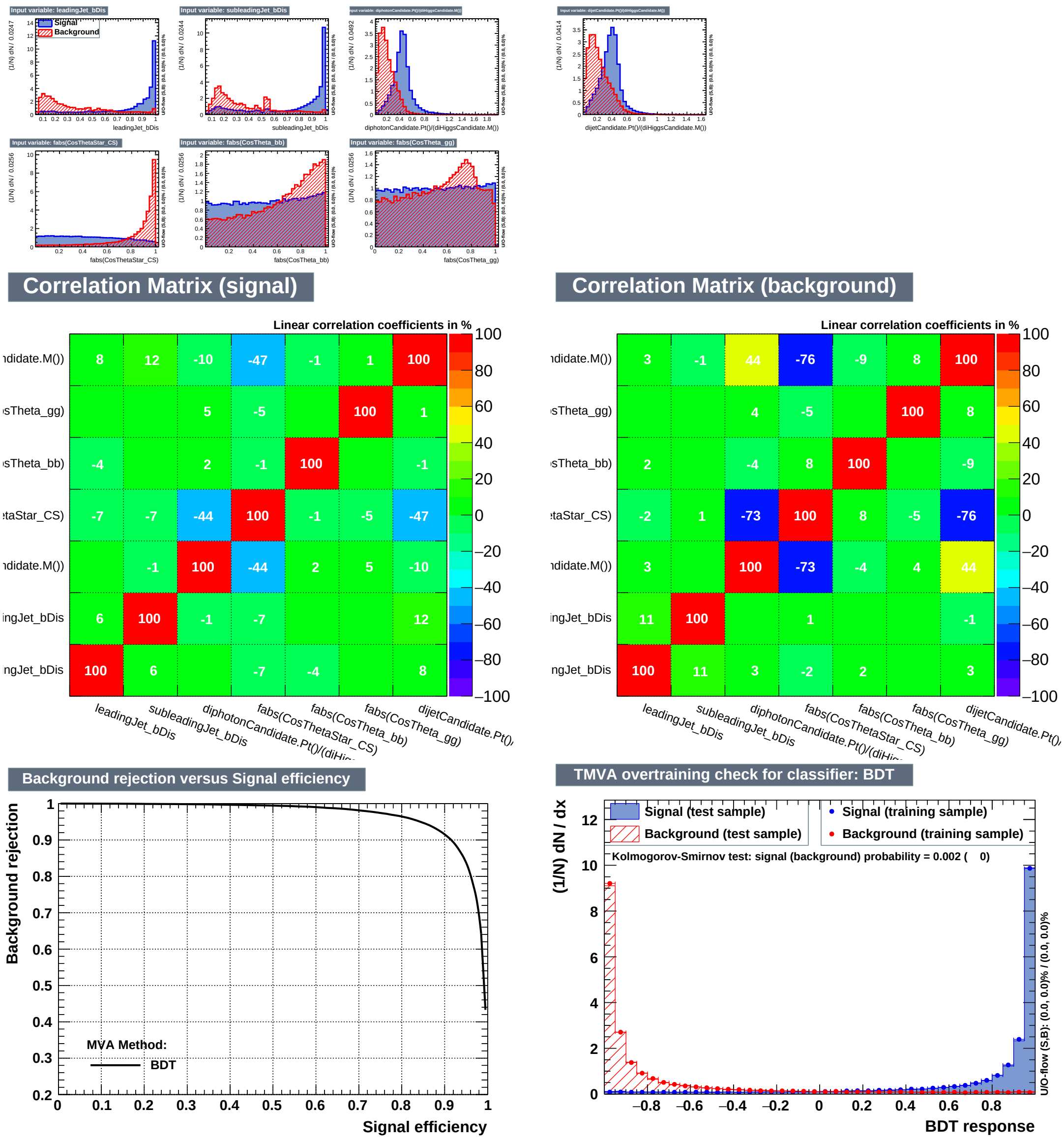

Figure 5.13: TMVA output plots for the High Mass Training.

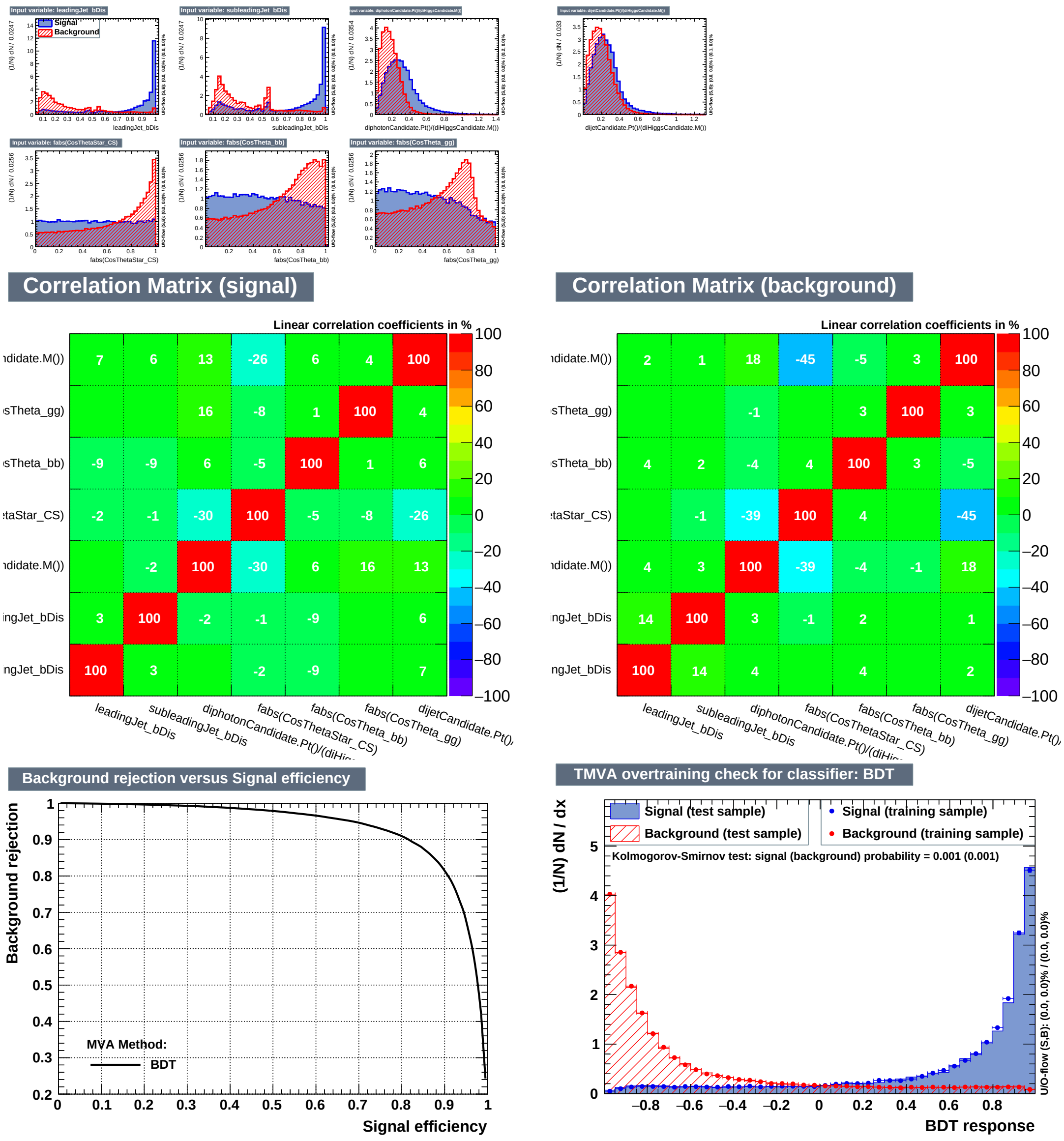

Figure 5.14: TMVA output plots for the Low Mass Training.

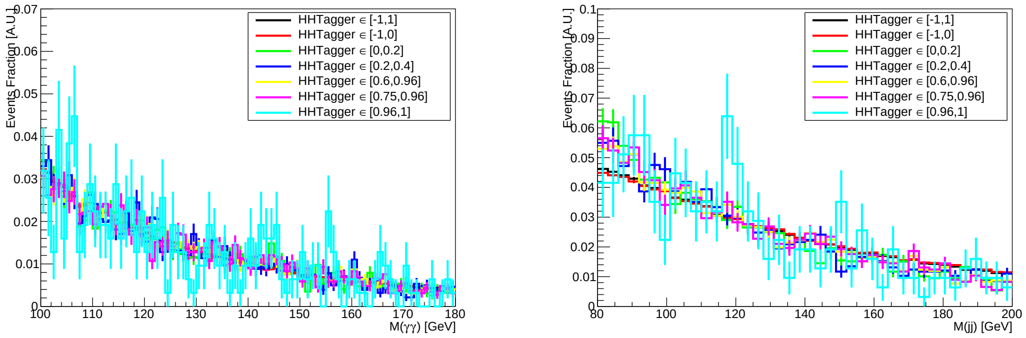

Figure 5.15: $M(\gamma\gamma)$ and $M(jj)$ in bins of HHTagger. Although the slope changes between bins, this effect does not influence the limit setting.

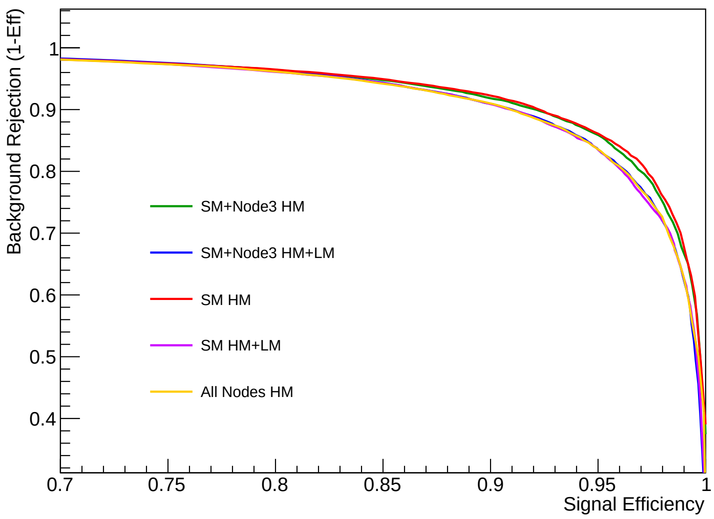

Figure 5.16: ROC curves with different signal hypotheses for training. The performance is evaluated on the high mass region, with the photon control region as background and SM HH as signal.

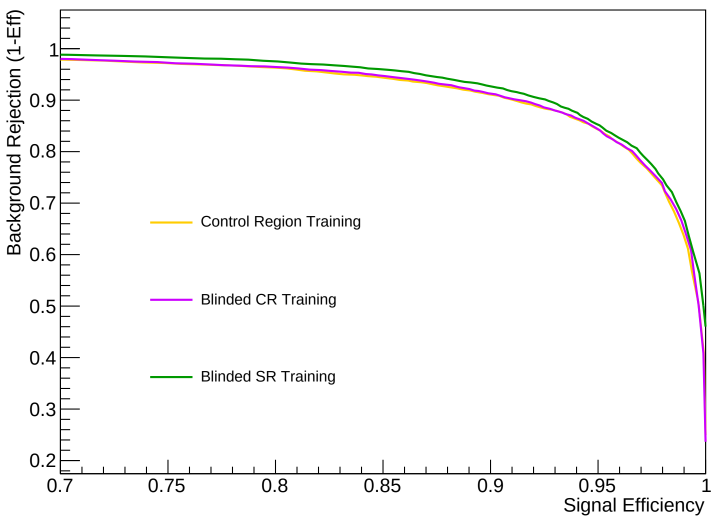

Figure 5.17: ROC curves with different background hypotheses for training. The performance is evaluated on the high mass region, with the blinded signal region as background and SM HH as signal.

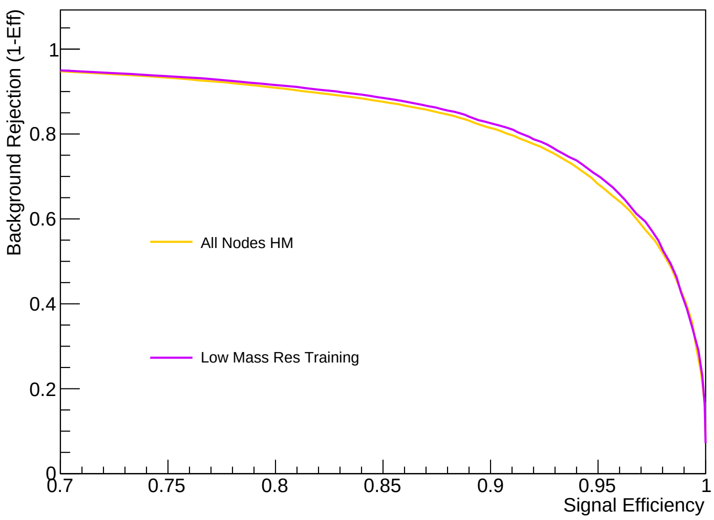

Figure 5.18: ROC curves with different signal hypotheses for training. The performance is evaluated on the high mass region, with the photon control region as background and Radion 300 GeV as signal.

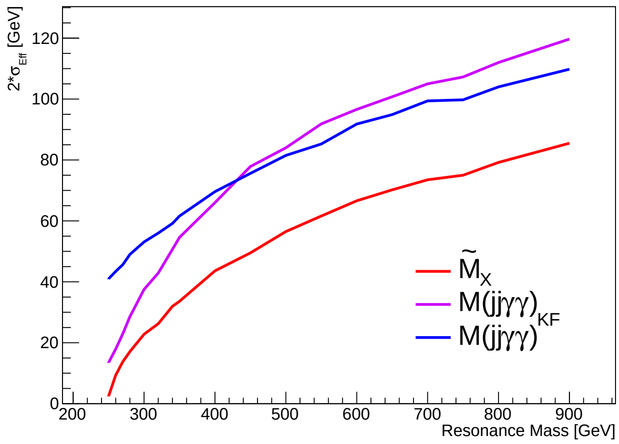

Figure 5.19: Different 4-body mass widths: $\tilde{M}_{\mathrm{X}}$, $M(jj\gamma\gamma)$ with kinematic fit, and $M(jj\gamma\gamma)$ with no extra corrections.

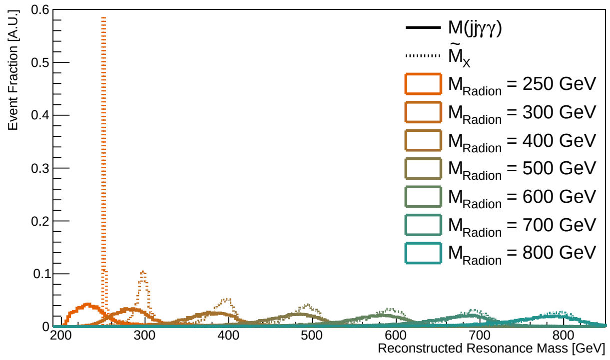

Figure 5.20: Different 4-body mass reconstructions: $\tilde{M}_{\mathrm{X}}$ (dotted line), $M(jj\gamma\gamma)$ with kinematic fit (dashed line), and $M(jj\gamma\gamma)$ with no extra correction (full line). Signals for different radion masses are shown. The normalizations are such that the non-corrected mass peaks at 1 (same normalization for different reconstructions in each mass point). This plot is made after full selection, in the b-tagging signal region (at least one medium b-tagged jet).

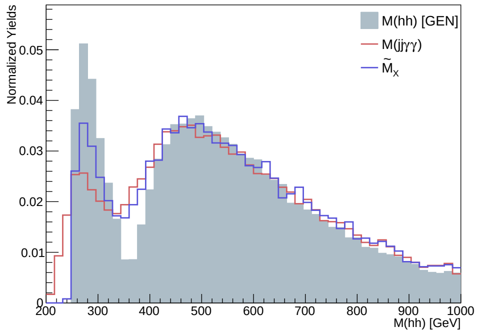

Figure 5.21: Behavior of $\tilde{M}_{\mathrm{X}}$, $M(jj\gamma\gamma)$ and GEN-level $M(hh)$. WARNING - THIS IS THE 2015 PLOT

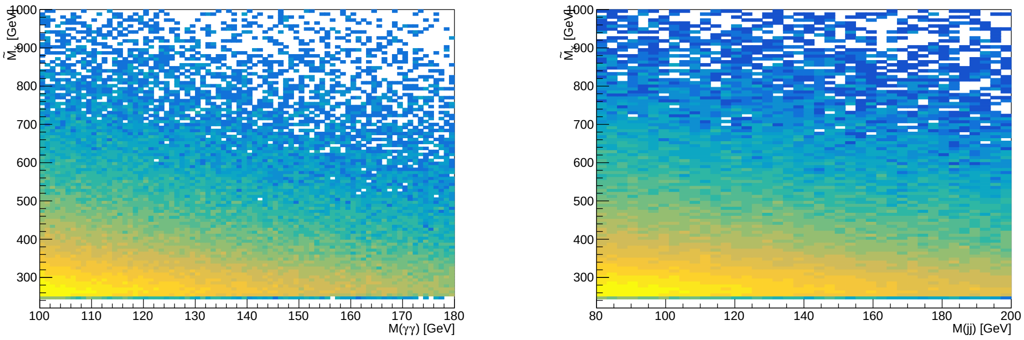

Figure 5.22: $\tilde{M}_{\mathrm{X}}$: $M(\gamma\gamma)$ and $\tilde{M}_{\mathrm{X}}$: $M(jj)$ in the photon control region, scaled to unity and Z-axis in log scale.

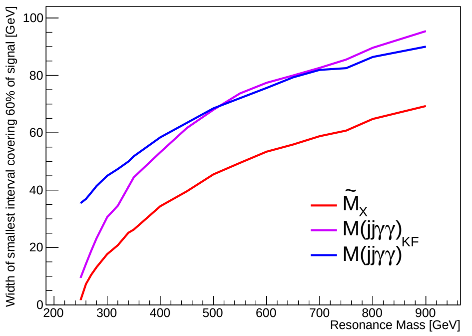

Figure 5.23: Mass window sizes as a function of the resonance mass.

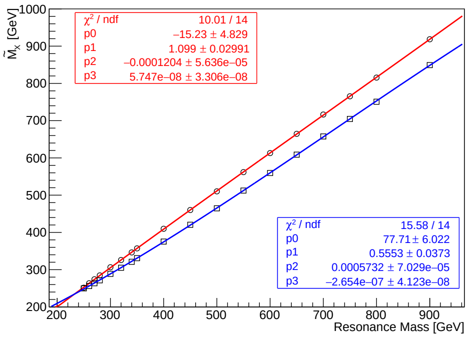

Figure 5.24: Mass window sizes as a function of the resonance mass.

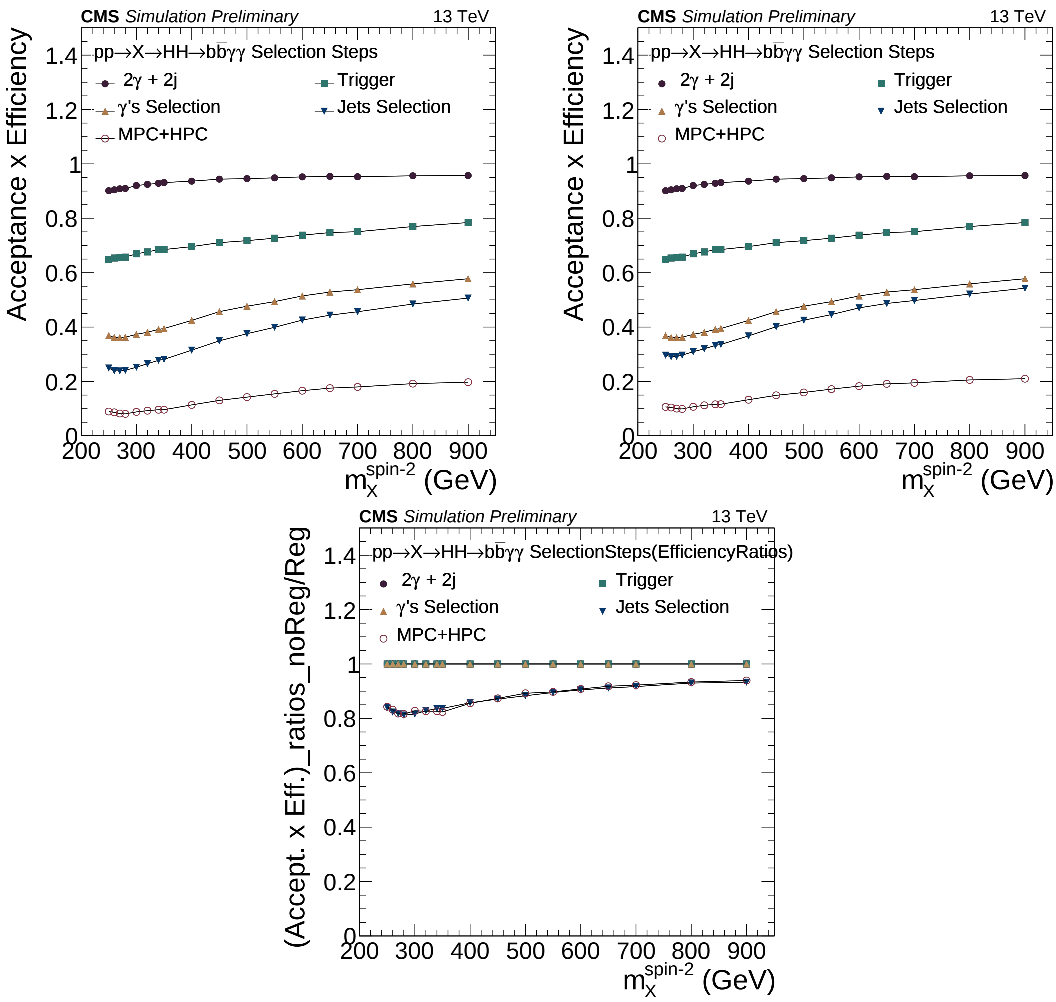

Figure 5.25: Graviton signal acceptance×efficiency for each cut (described in text) on the top left plot, the bjet regression is applied on the top right and the ratio of the cutflows on the bottom.

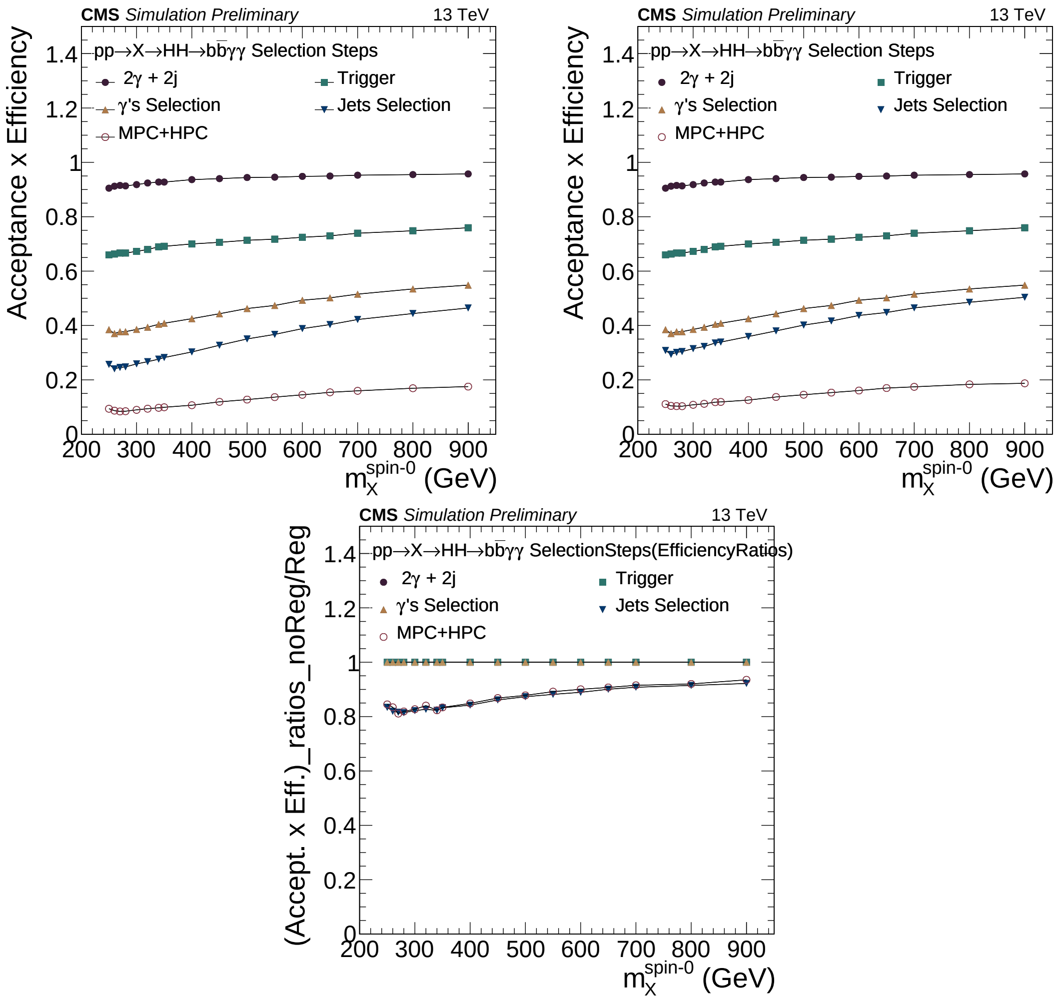

Figure 5.26: Radion signal acceptance×efficiency for each cut (described in text) on the top left plot, the bjet regression is applied on the top right and the ratio of the cutflows on the bottom.

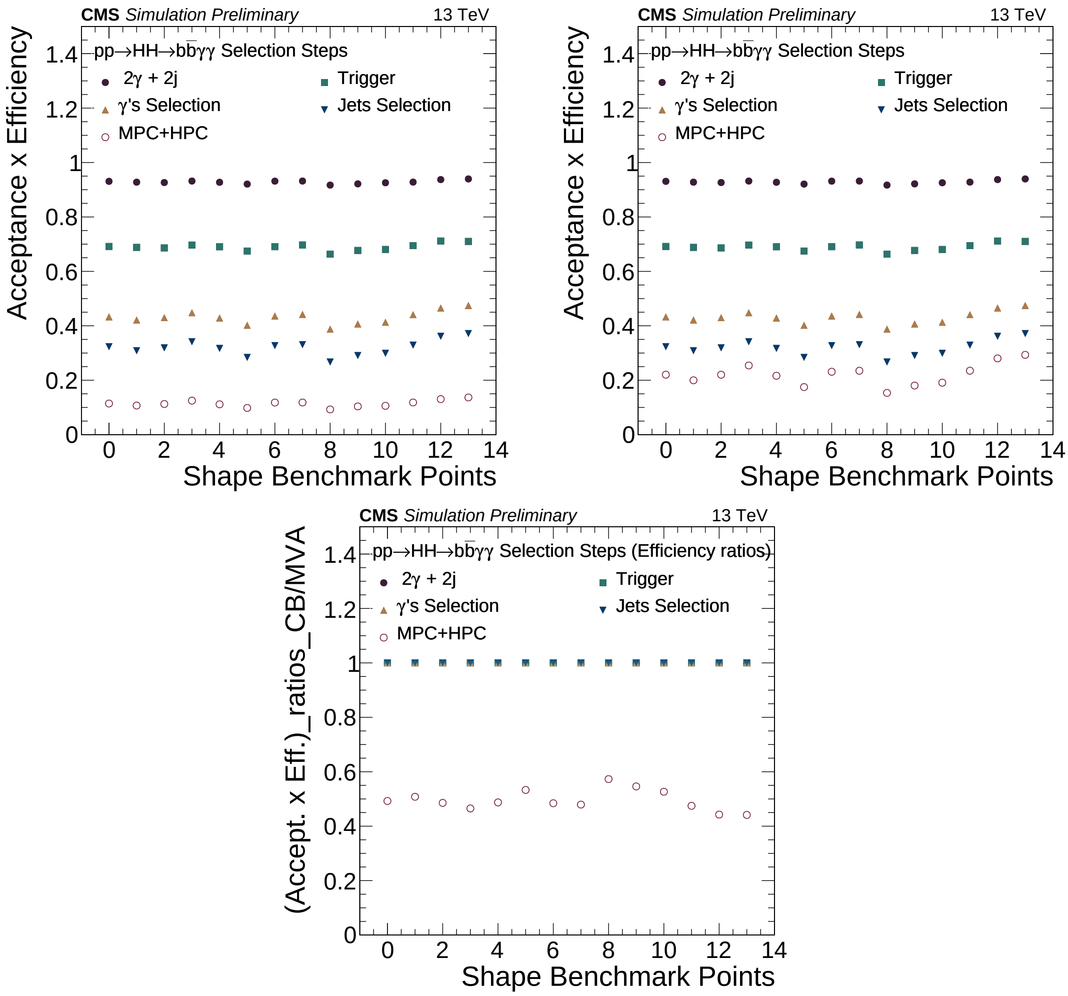

Figure 5.27: Non-resonant acceptance x efficiency. Cut based categorization on the top left, MVA based categorization on the top right (analysis version) and the ratio of the two on the bottom.

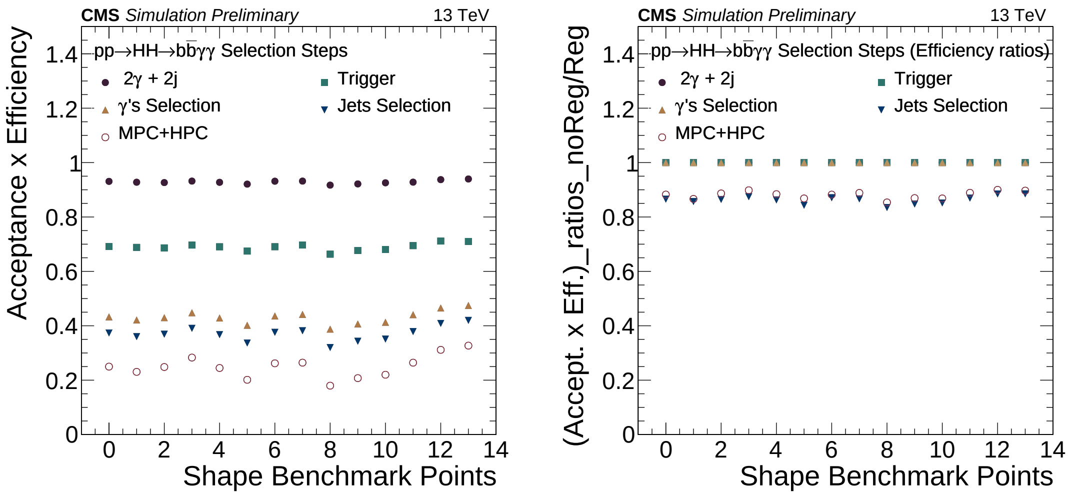

Figure 5.28: Non-resonant acceptance x efficiency. Jet energy regression applied in addition to MVA based categorization on the left, ratio (bjetReg.+MVA)/MVA on the right (analysis version).

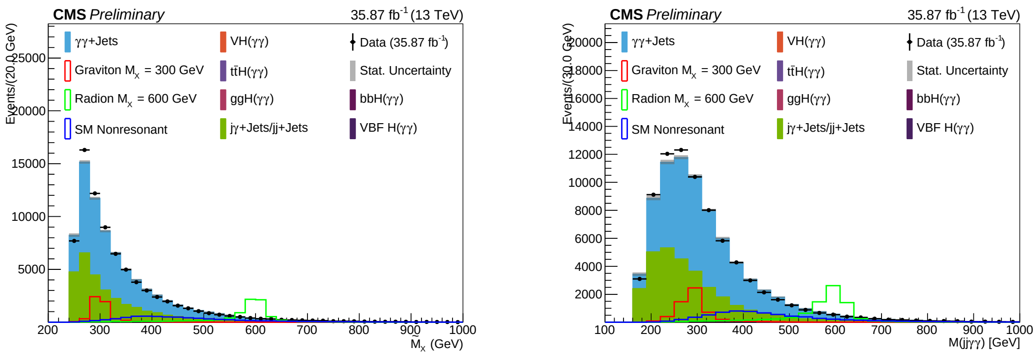

Figure 5.29: Distributions for the blinded signal region.

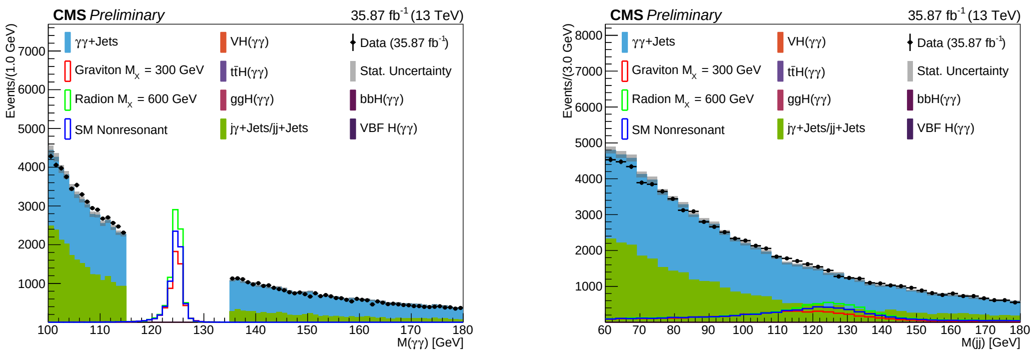

Figure 5.30: Distributions for the blinded signal region.

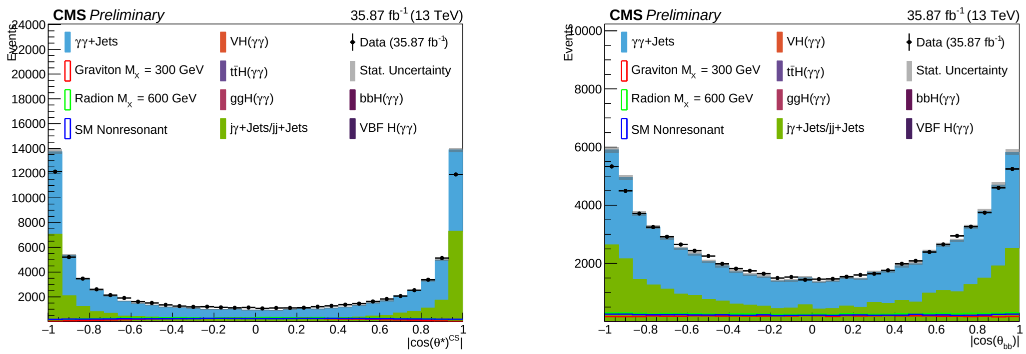

Figure 5.31: Distributions for the blinded signal region.

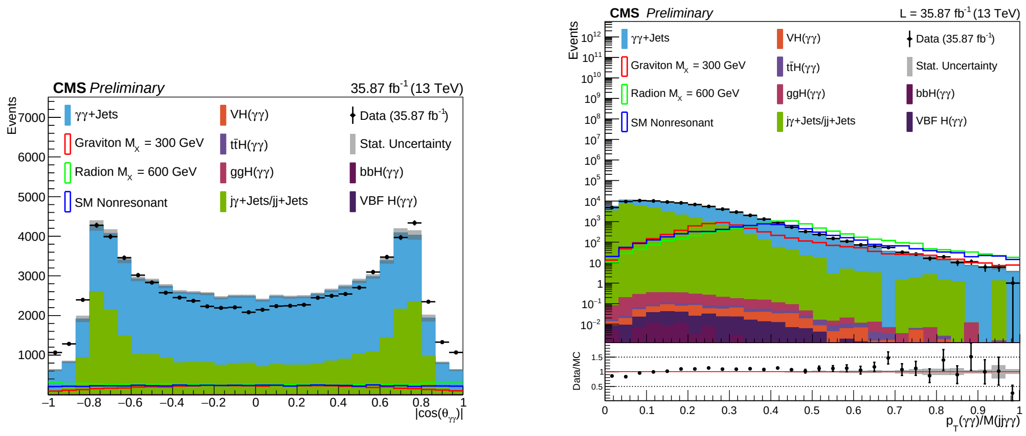

Figure 5.32: Distributions for the blinded signal region.

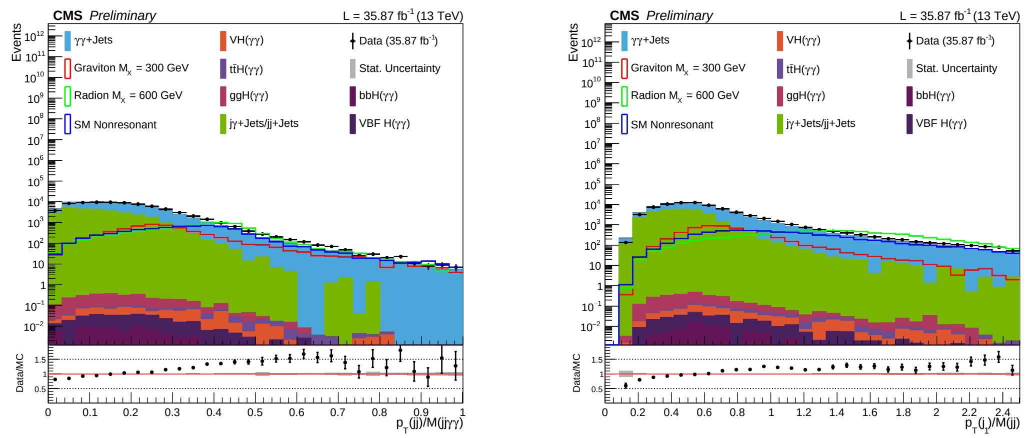

Figure 5.33: Distributions for the blinded signal region.

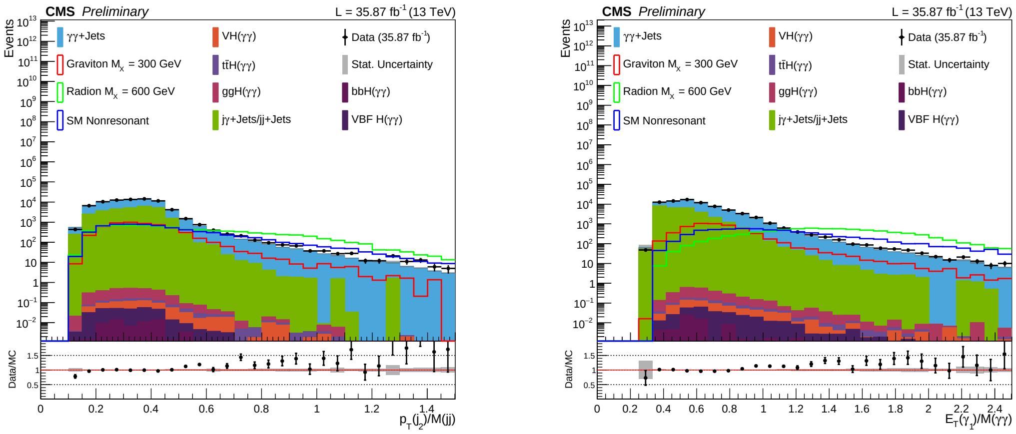

Figure 5.34: Distributions for the blinded signal region.

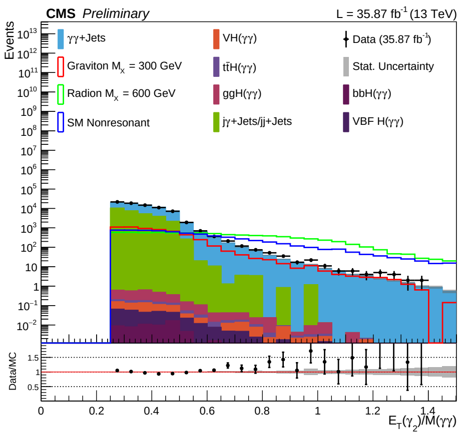

Figure 5.35: Distributions for the blinded signal region.

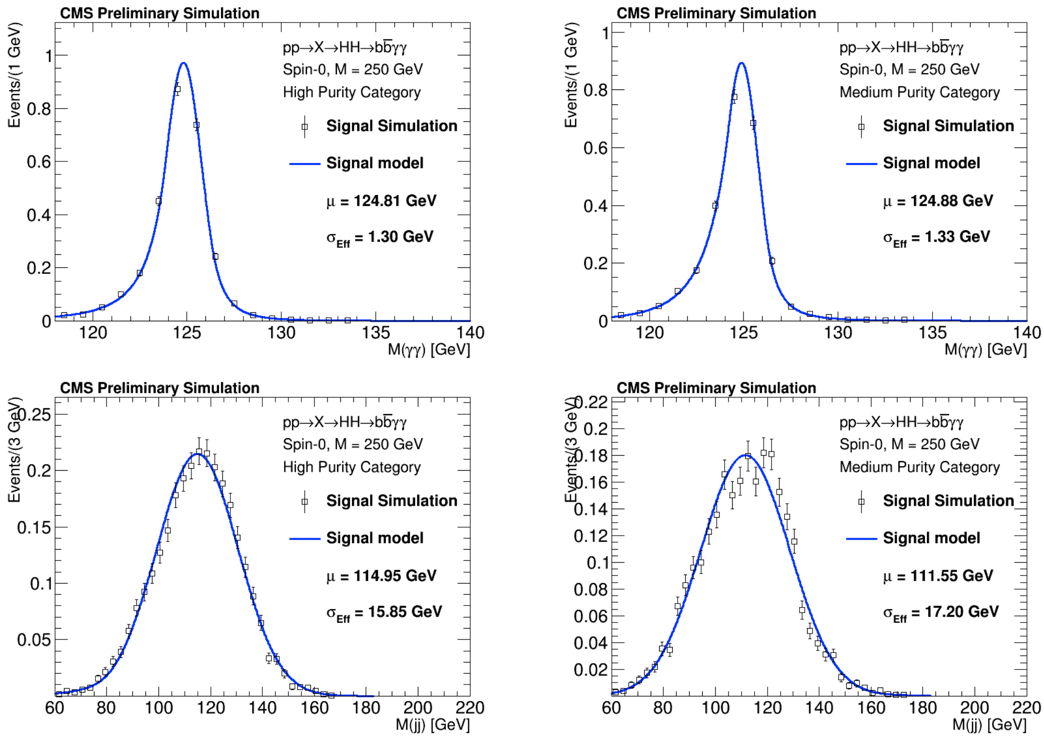

Figure 5.36: Signal fits for the Radion 250 GeV sample after full analysis selection, in High and Medium purity categories.

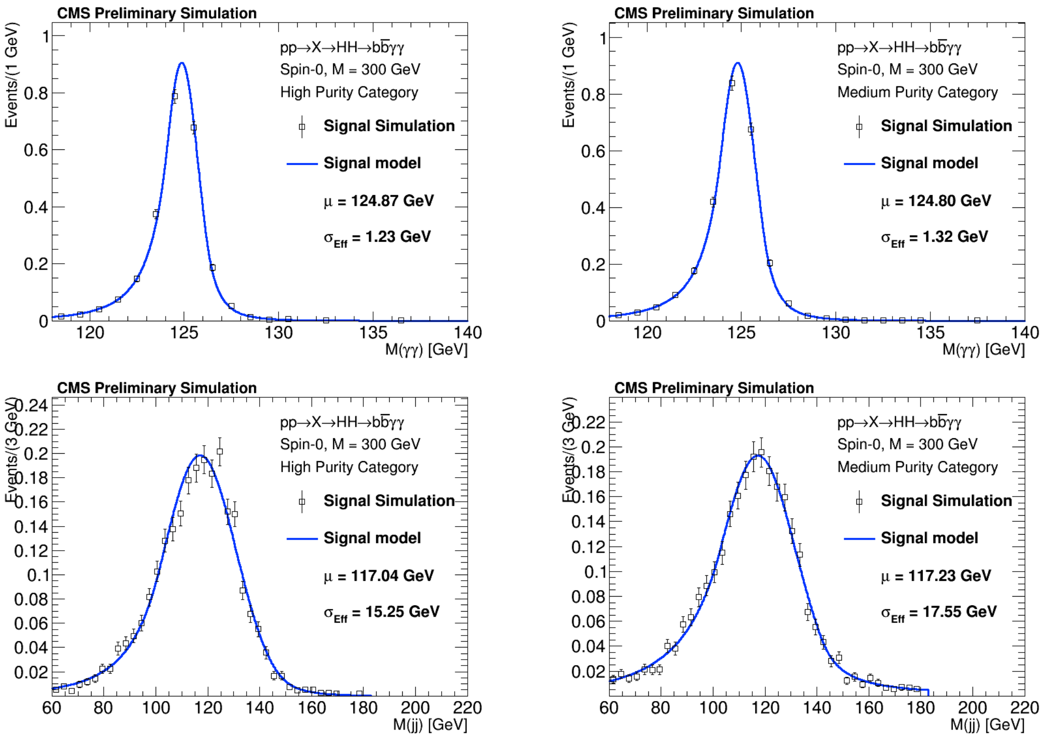

Figure 5.37: Signal fits for the Radion 300 GeV sample after full analysis selection, in High and Medium purity categories.

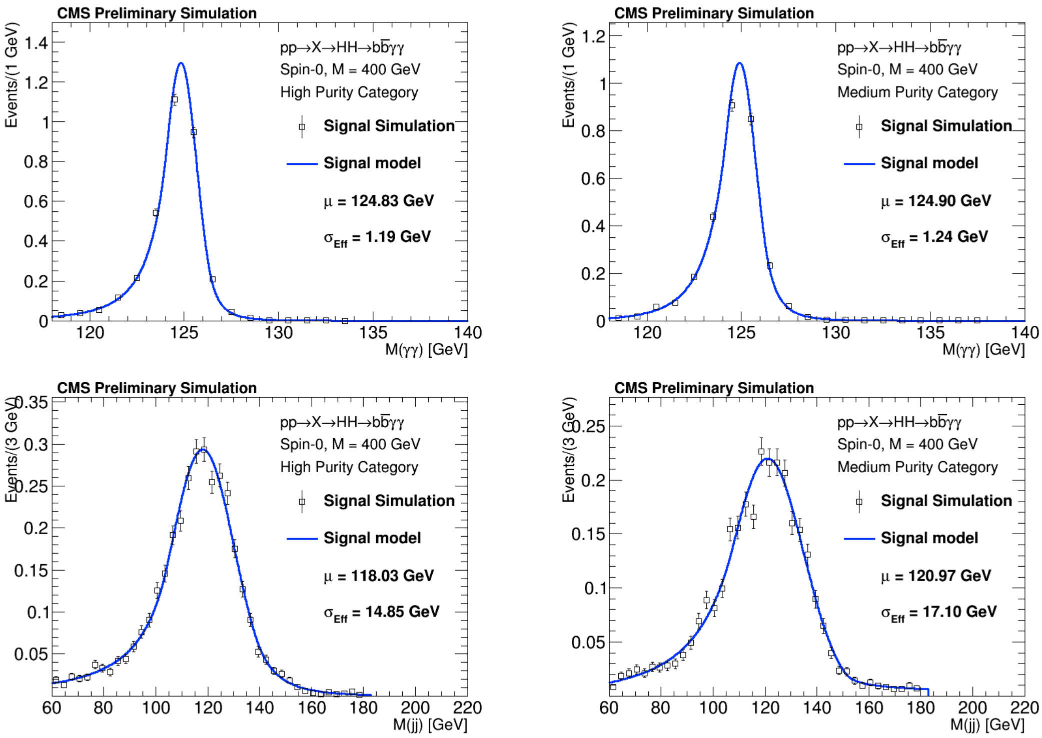

Figure 5.38: Signal fits for the Radion 400 GeV sample after full analysis selection, in High and Medium purity categories.

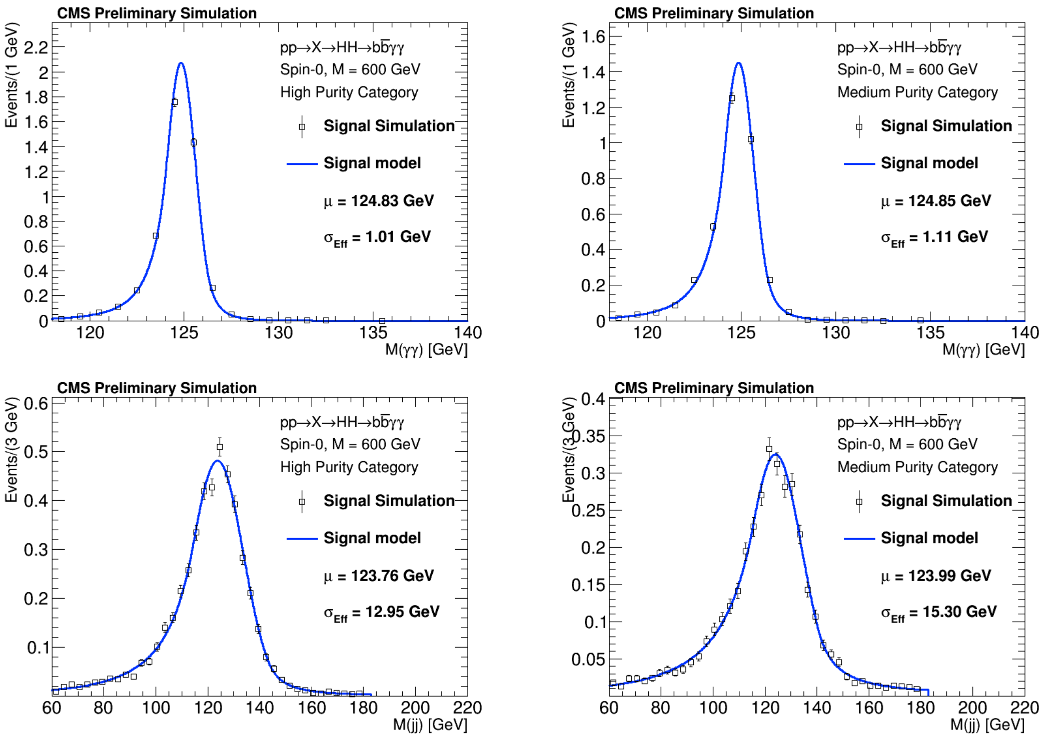

Figure 5.39: Signal fits for the Radion 600 GeV sample after full analysis selection, in High and Medium purity categories.

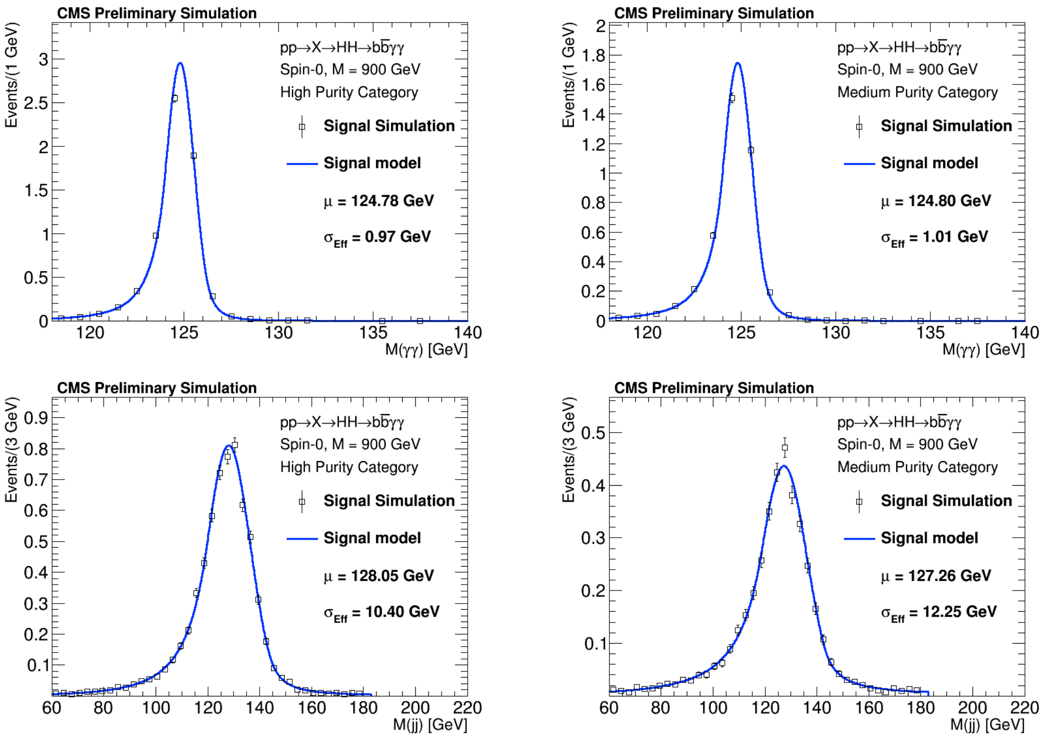

Figure 5.40: Signal fits for the Radion 900 GeV sample after full analysis selection, in High and Medium purity categories.

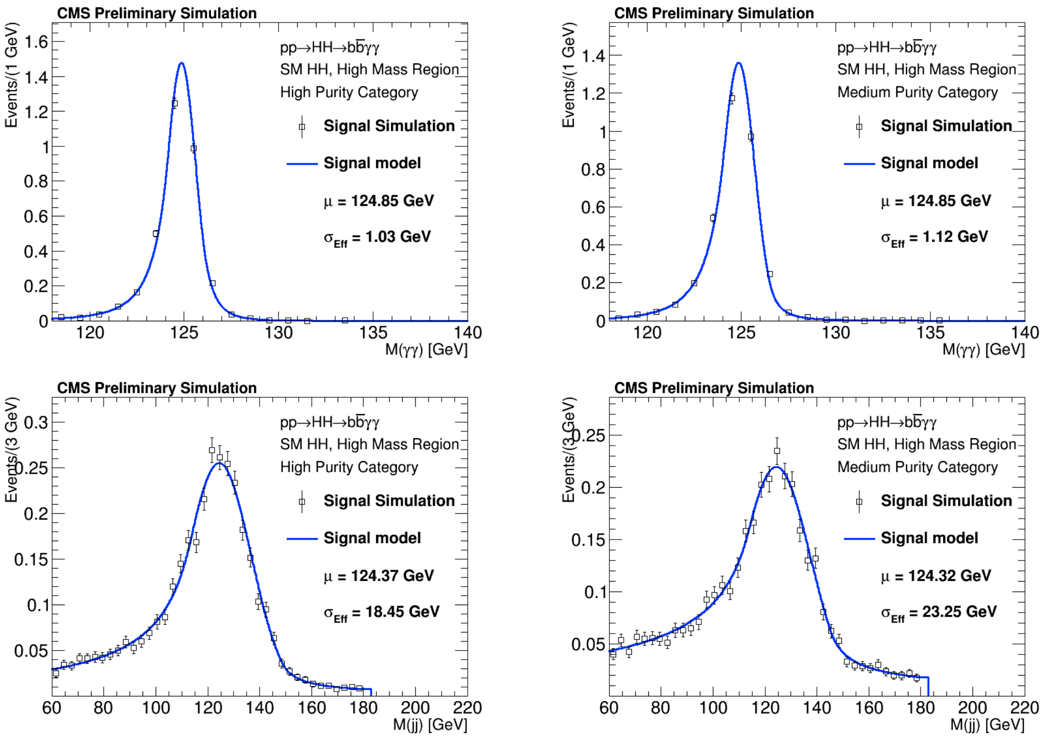

Figure 5.41: Signal fits for the SM HH non-resonant sample after full analysis selection, in categories 0 and 1, for high mass category.

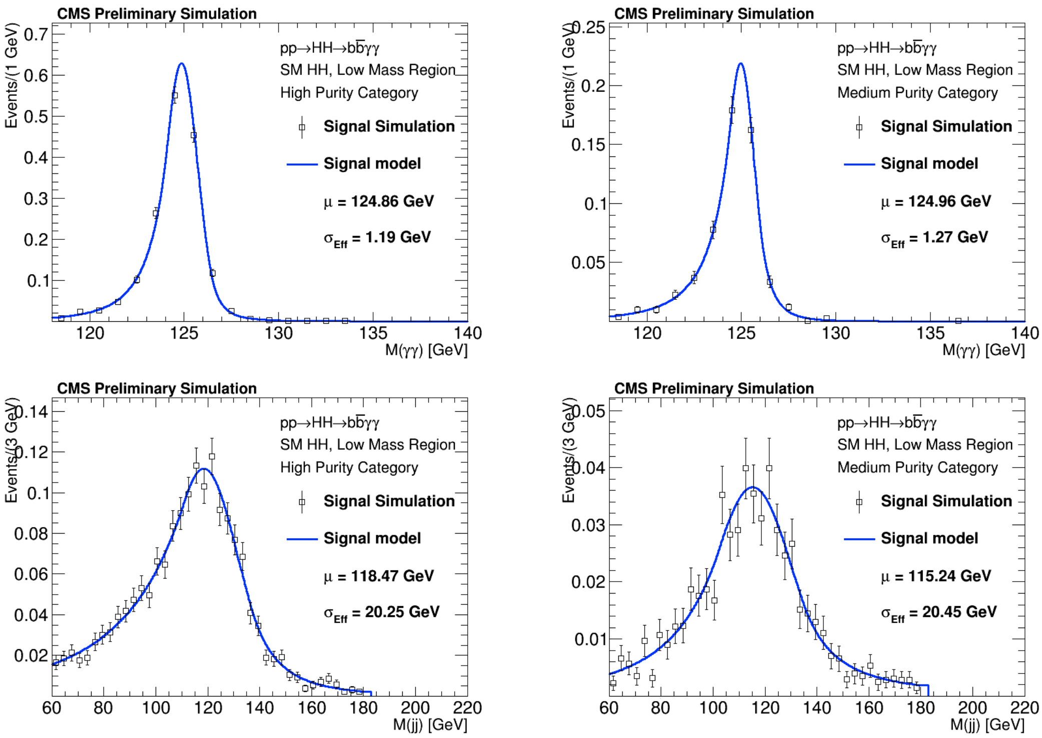

Figure 5.42: Signal fits for the SM HH non-resonant sample after full analysis selection, in categories 0 and 1, for low mass category.

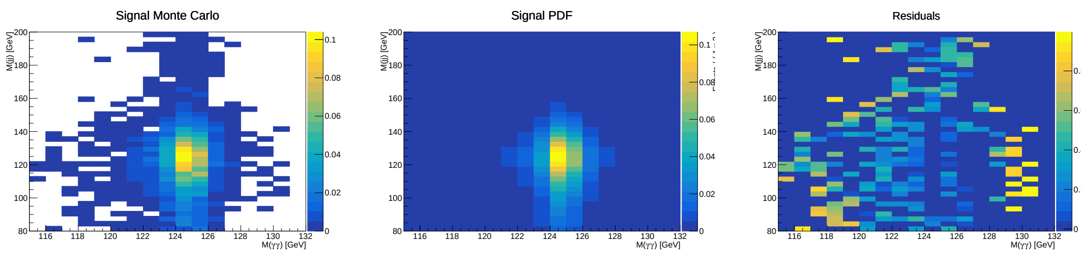

Figure 5.43: 2D distributions of the signal MC (left), fitted PDF model (center) and 2D residuals (right) for the High Mass-High Purity Category non-resonant selection.

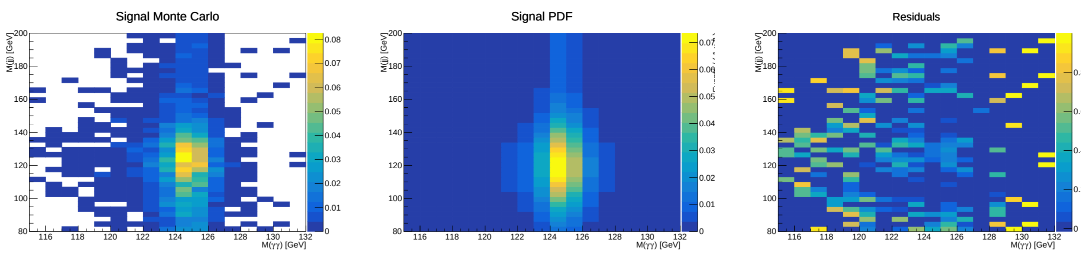

Figure 5.44: 2D distributions of the signal MC (left), fitted PDF model (center) and 2D residuals (right) for the High Mass-Medium Purity Category non-resonant selection.

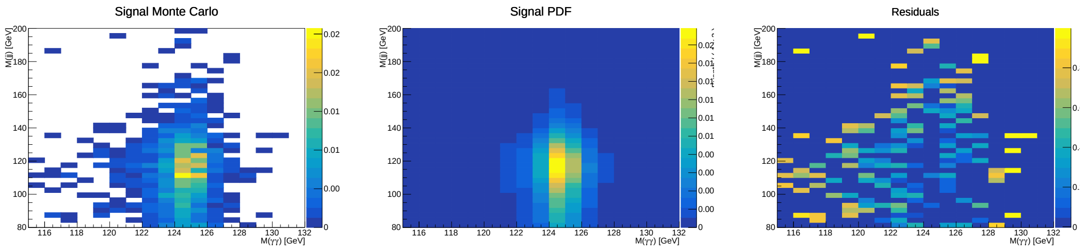

Figure 5.45: 2D distributions of the signal MC (left), fitted PDF model (center) and 2D residuals (right) for the Low Mass-High Purity Category non-resonant selection.

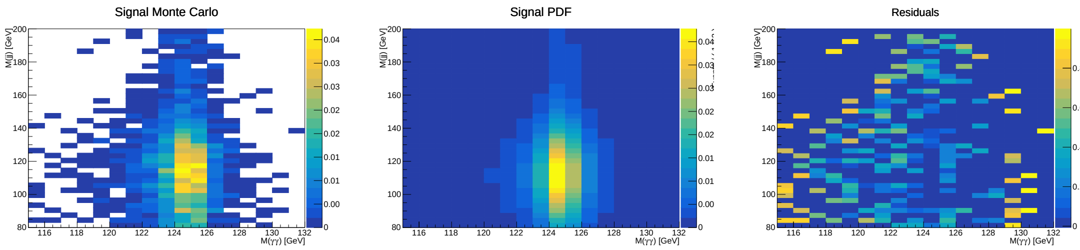

Figure 5.46: 2D distributions of the signal MC (left), fitted PDF model (center) and 2D residuals (right) for the Low Mass-Medium Purity Category non-resonant selection.

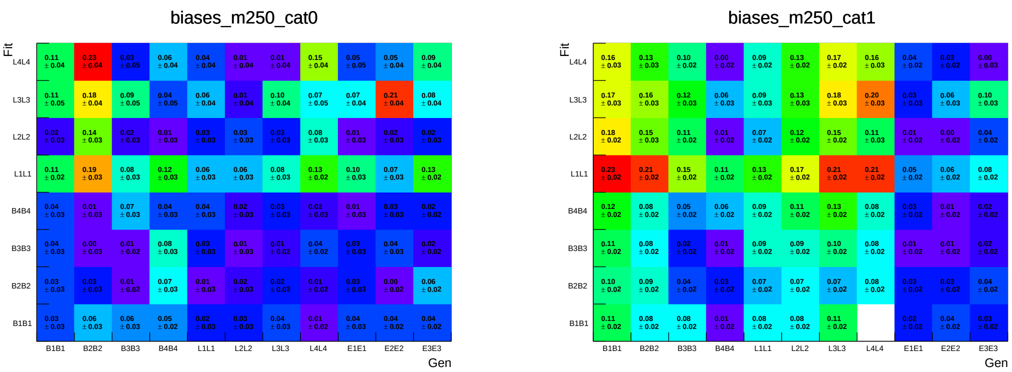

Figure 5.47: Signal fits for the SM HH non-resonant sample after full analysis selection, in categories 0 and 1, for high mass category.

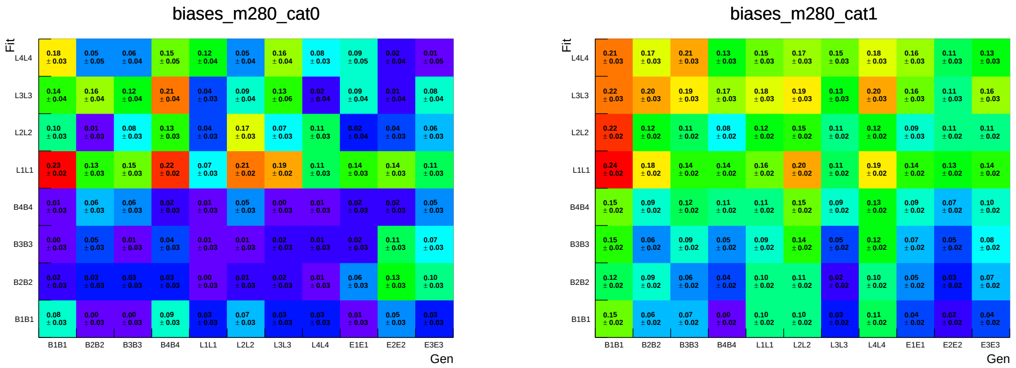

Figure 5.48: Signal fits for the SM HH non-resonant sample after full analysis selection, in categories 0 and 1, for high mass category.

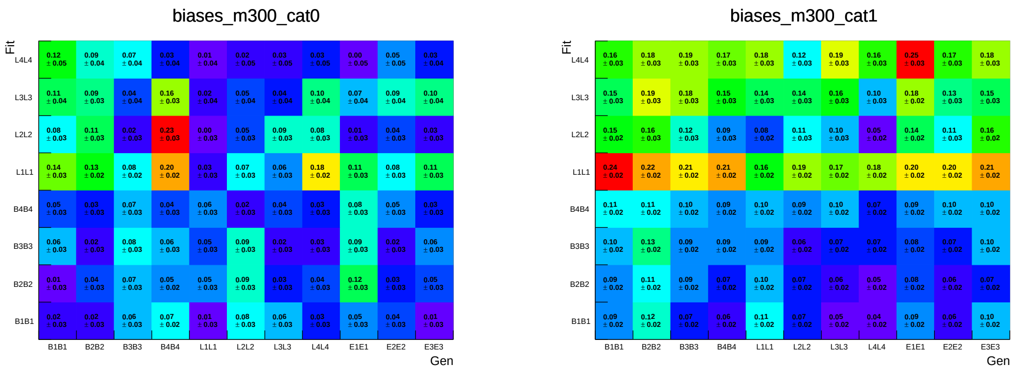

Figure 5.49: Signal fits for the SM HH non-resonant sample after full analysis selection, in categories 0 and 1, for high mass category.

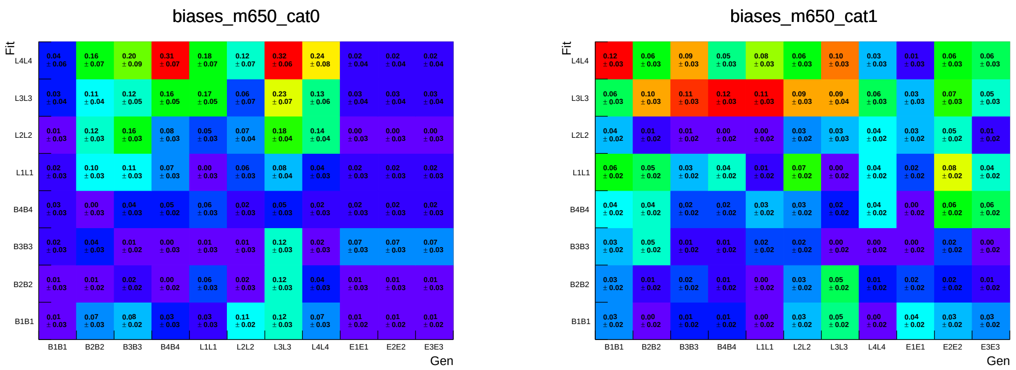

Figure 5.50: Signal fits for the SM HH non-resonant sample after full analysis selection, in categories 0 and 1, for high mass category.

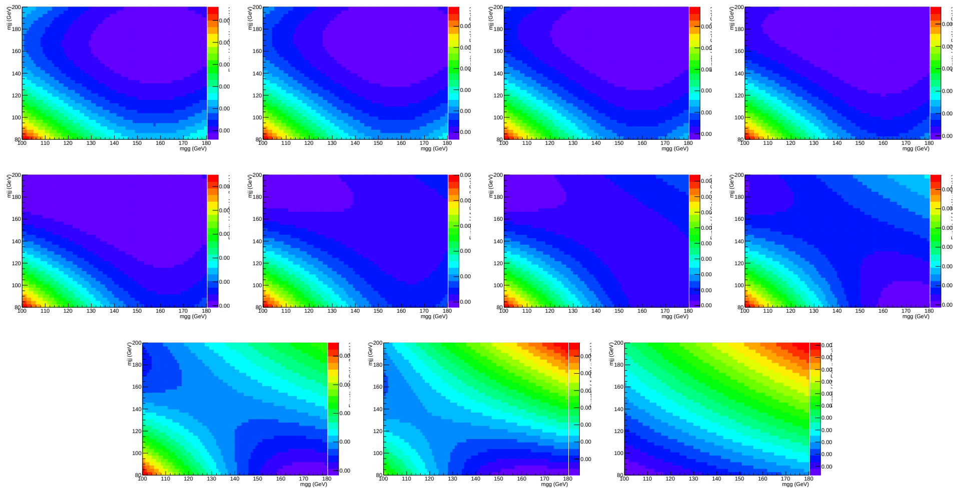

Figure 5.51: 2D distributions of $g_{corr}(x, y)$ with α from 0 to 1, from top to bottom, left to right.

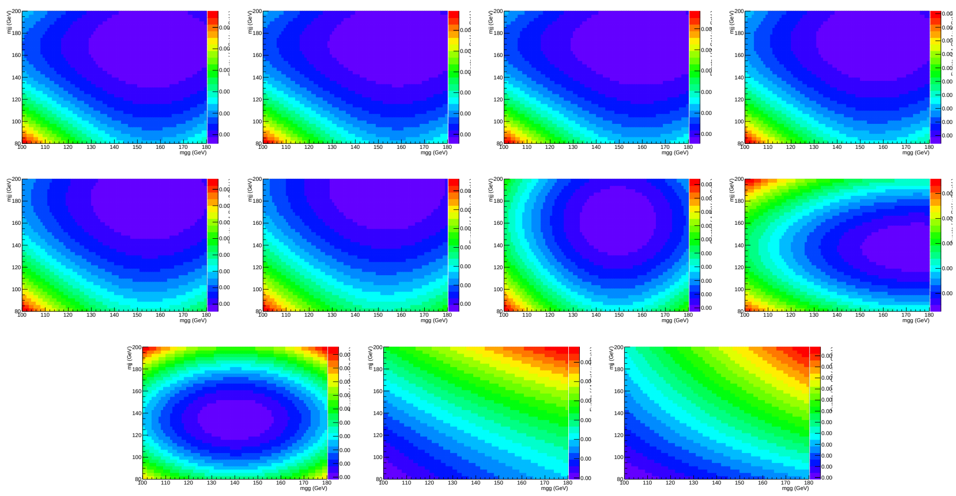

Figure 5.52: 2D distributions of $g(x, y)$ fitted to the Asimov datasets produced with $g_{corr}(x, y)$ with α from 0 to 1, from top to bottom, left to right.

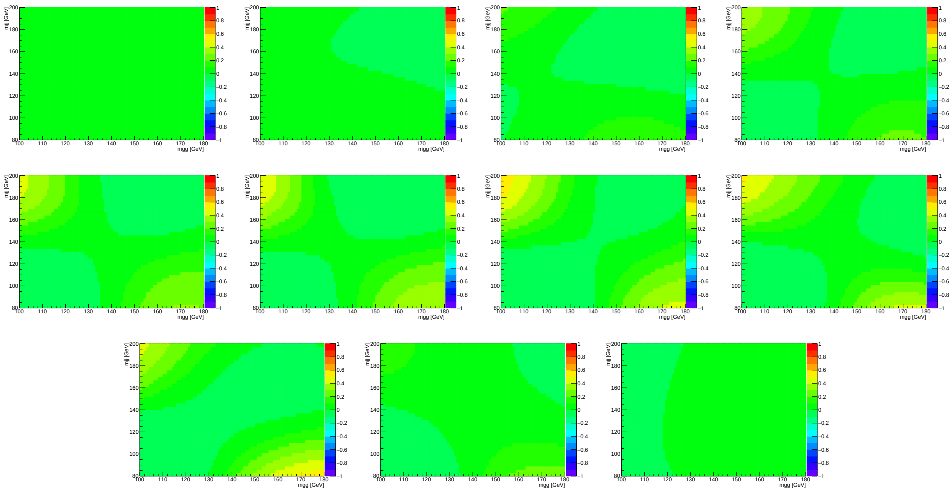

Figure 5.53: 2D residuals comparing distributions of $g(x, y)$ fitted to the Asimov datasets produced with $g_{corr}(x, y)$ with α from 0 to 1 and the dataset , from top to bottom, left to right. The background normalization is 200 events.

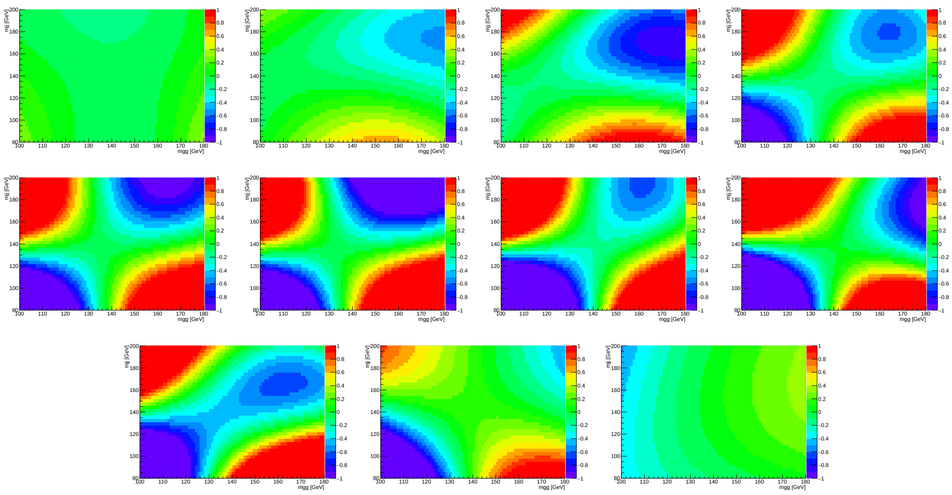

Figure 5.54: 2D residuals comparing distributions of $g(x, y)$ fitted to the Asimov datasets produced with $g_{corr}(x, y)$ with α from 0 to 1 and the dataset , from top to bottom, left to right. The background normalization is 100k events.

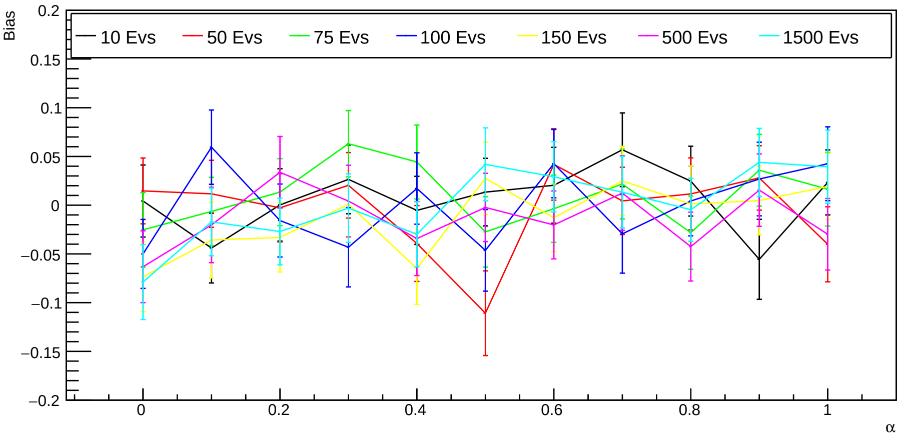

Figure 5.55: Relative bias on measuring the signal with $g(x, y)$ on toys created with $g_{corr}(x, y)$ with α from 0 to 1, for different background normalization hypotheses.

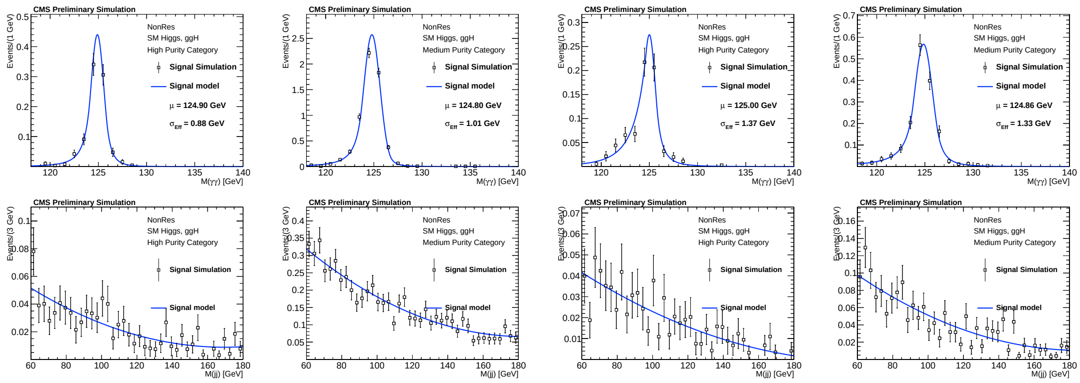

Figure 5.56: Higgs model fit to Higgs Monte Carlo (ggH).

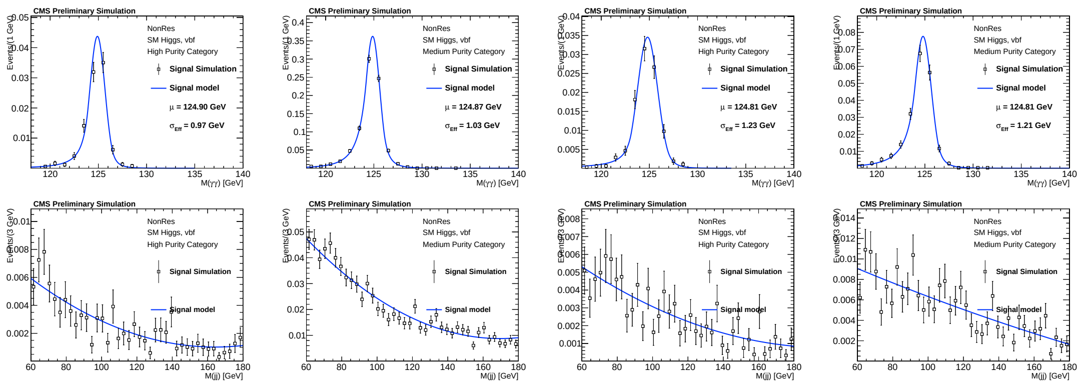

Figure 5.57: Higgs model fit to Higgs Monte Carlo (VBF).

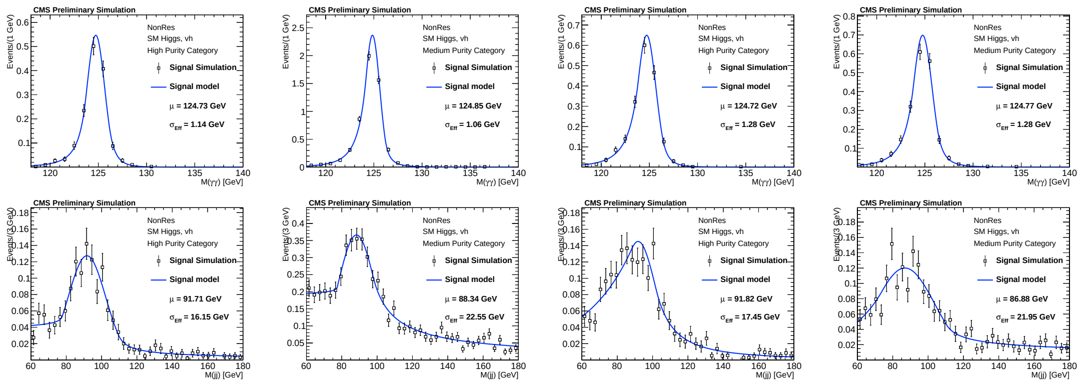

Figure 5.58: Higgs model fit to Higgs Monte Carlo (VH).

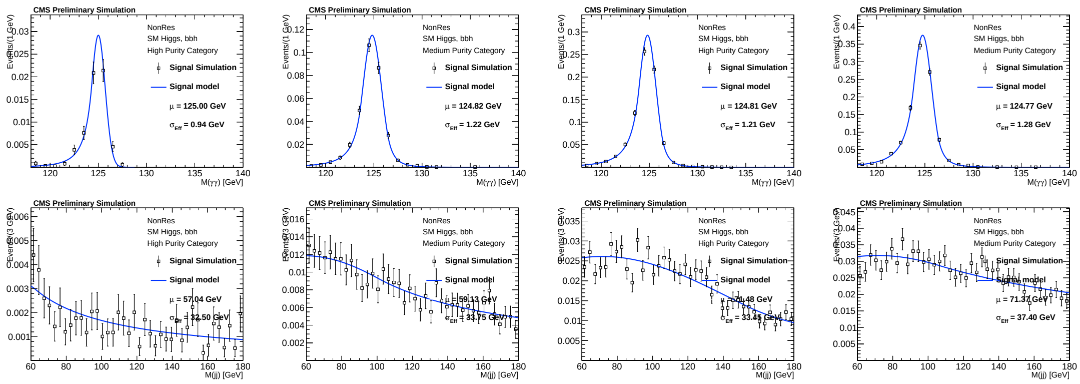

Figure 5.59: Higgs model fit to Higgs Monte Carlo (bbH).

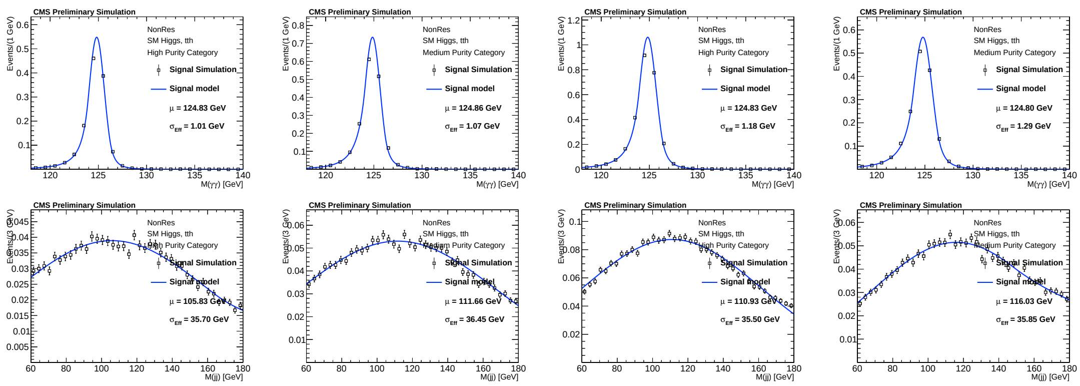

Figure 5.60: Higgs model fit to Higgs Monte Carlo (ttH).

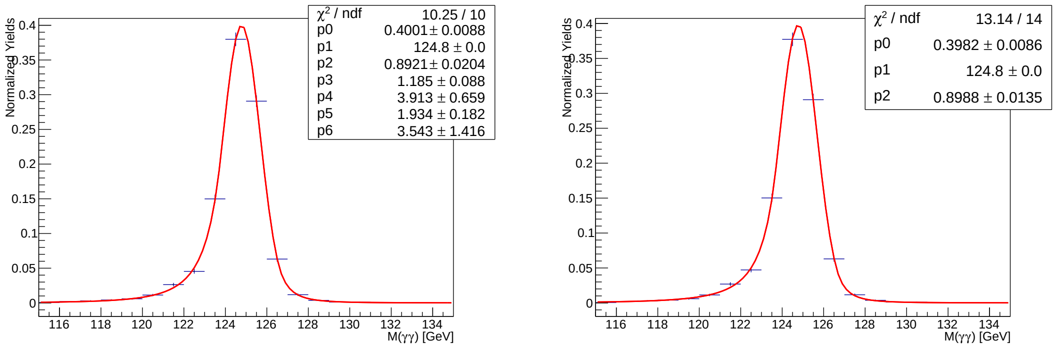

Figure 5.61: Signal fits for the High Mass Medium purity categories, in the un-smeared MC with floating tails (left) and on the smeared MC with fixed tails (right). The tail parameters on the right are fixed to their values on the left.

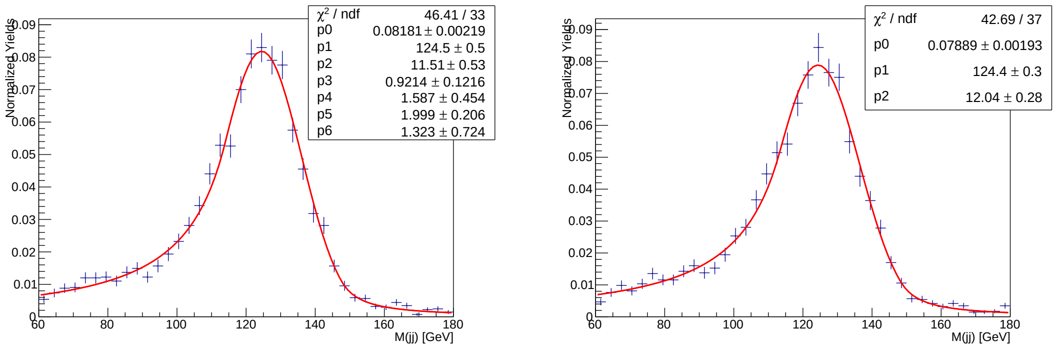

Figure 5.62: Signal fits for the High Mass Medium Purity category, in the un-smeared MC with floating tails (left) and on the smeared MC with fixed tails (right). The tail parameters on the right are fixed to their values on the left.

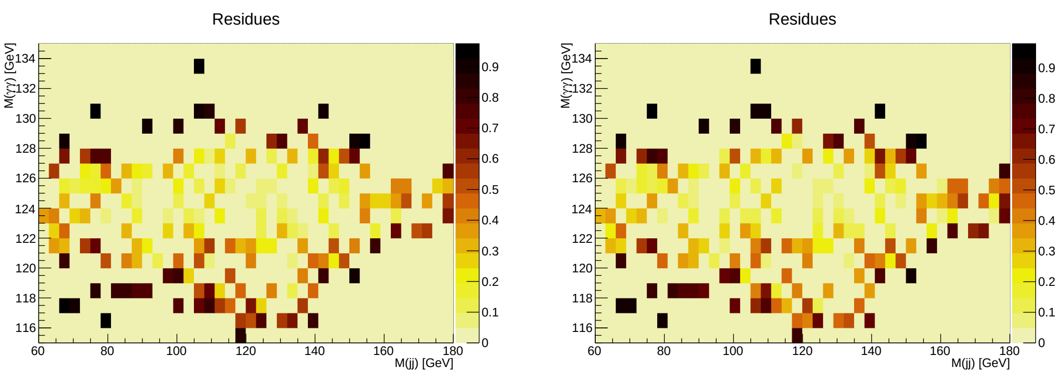

Figure 5.63: Residuais comparing the floating signal PDF fit to the smeared MC (left) and the fixed tails PDF fit to the smeared MC (right) in the High Mass Medium Purity category.

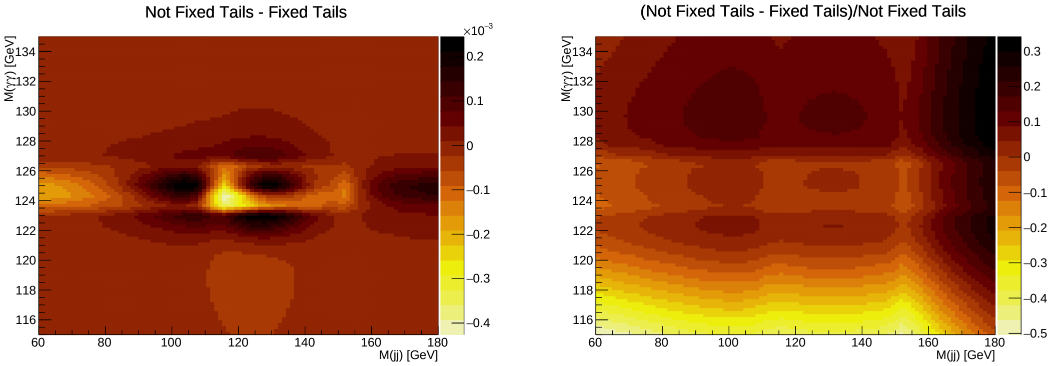

Figure 5.64: Comparison between fixed and floating PDF shapes when fitting the smeared MC.

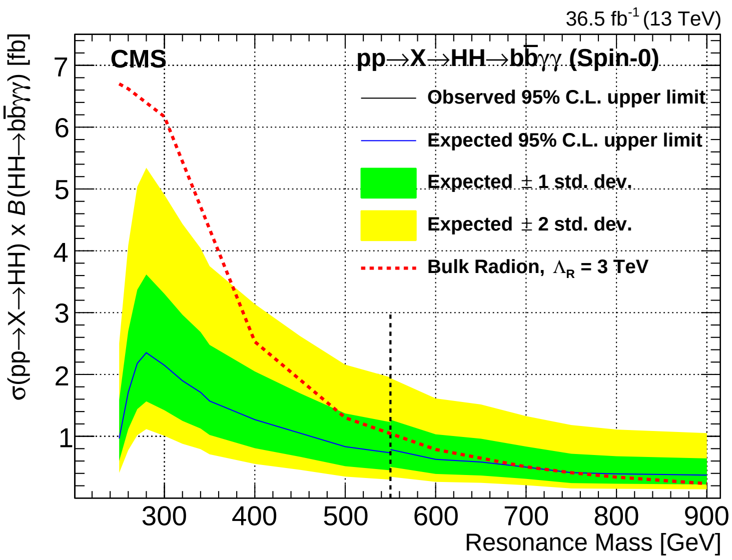

Figure 5.65: Limits on spin-0 resonances.

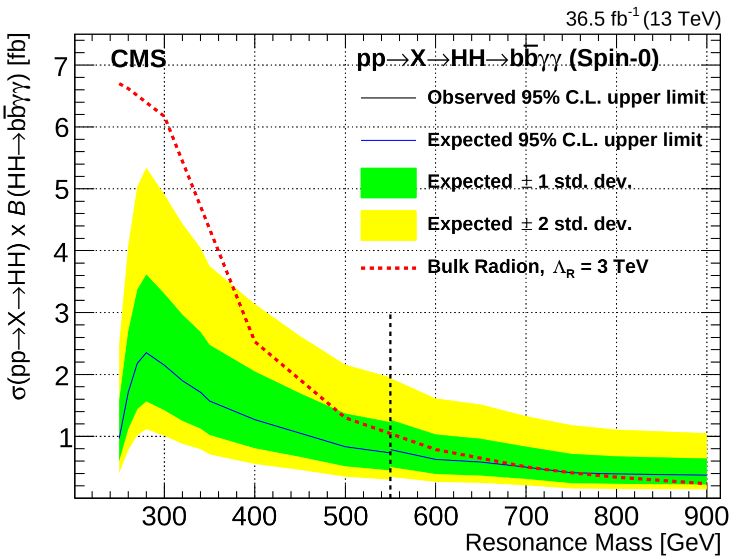

Figure 5.66: Limits on spin-2 resonances.

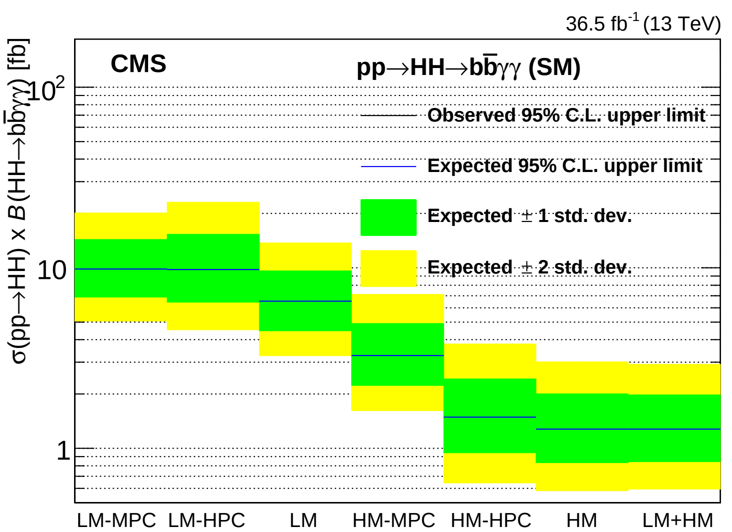

Figure 5.67: SM-like non-resonant limits.

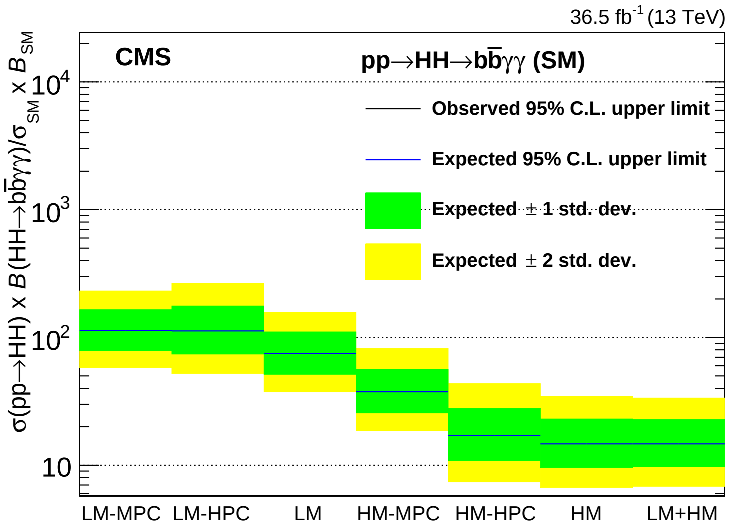

Figure 5.68: SM-like non-resonant limies normalized to SM cross section.

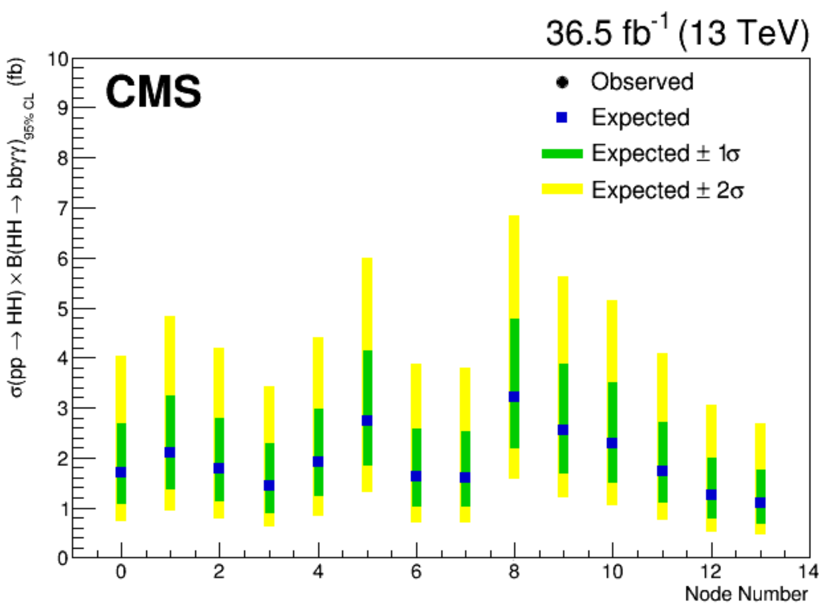

Figure 5.69: Limits for Nodes specified in Table 5.1.

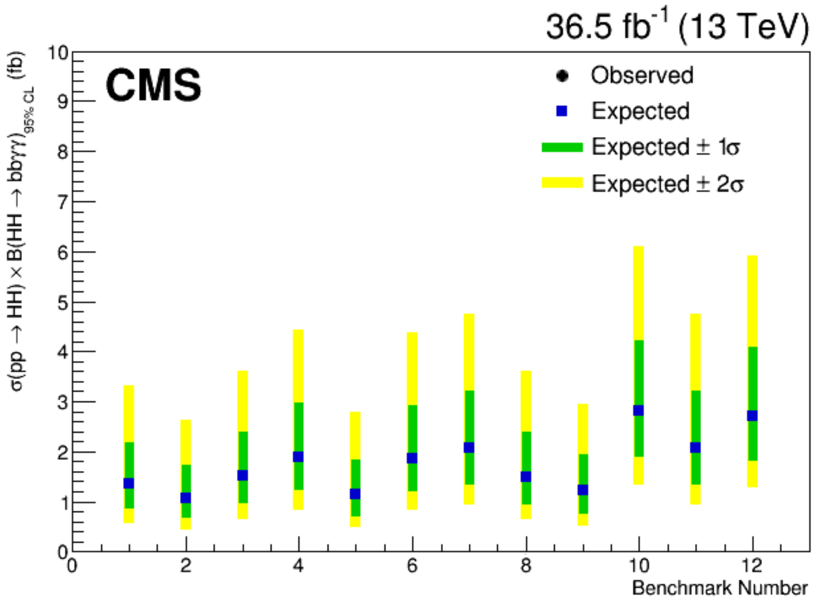

Figure 5.70: Limits for Benchmarks described in Sec. 5.2.2 in Table 5.2.

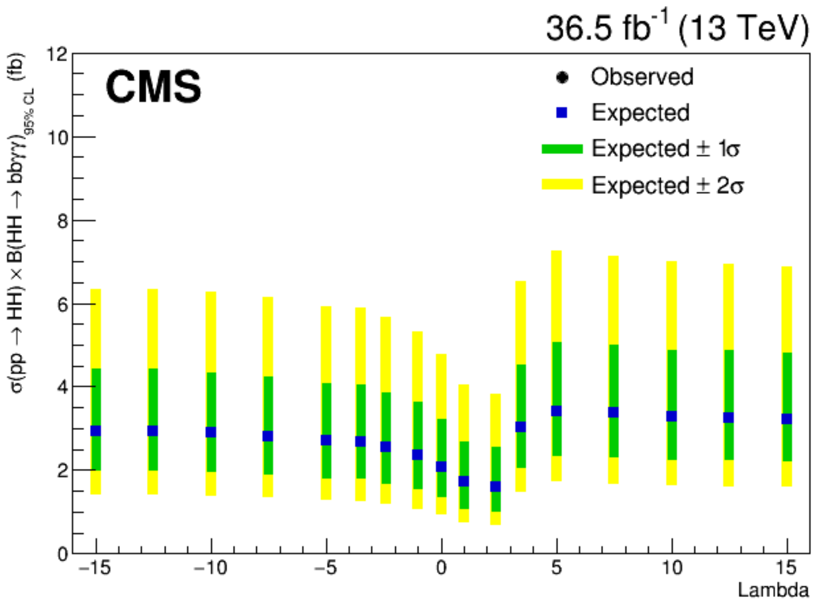

Figure 5.71: Upper limits for the BSM models with varying κ_λ parameter, while others fixed to their SM values.

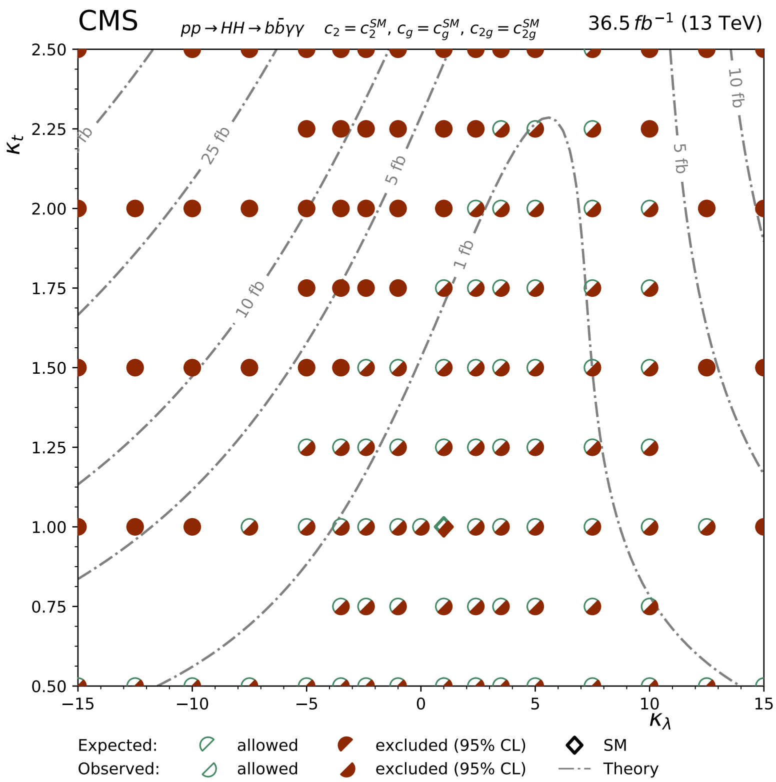

Figure 5.72: Upper limits for the BSM models with varying $\kappa_\lambda - \kappa_t$ parameters, while other parameters are fixed to their SM values.

Chapter 6

Conclusions

Lorem ipsum dolor sit amet, consectetur adipiscing elit, sed do eiusmod tempor incididunt ut labore et dolore magna aliqua. Ut enim ad minim veniam, quis nostrud exercitation ullamco laboris nisi ut aliquip ex ea commodo consequat. Duis aute irure dolor in reprehenderit in voluptate velit esse cillum dolore eu fugiat nulla pariatur. Excepteur sint occaecat cupidatat non proident, sunt in culpa qui officia deserunt mollit anim id est laborum.

Einstein's paper: [**?**]

Appendix A

Sample Title

Lorem ipsum dolor sit amet, consectetur adipiscing elit, sed do eiusmod tempor incididunt ut labore et dolore magna aliqua. Ut enim ad minim veniam, quis nostrud exercitation ullamco laboris nisi ut aliquip ex ea commodo consequat. Duis aute irure dolor in reprehenderit in voluptate velit esse cillum dolore eu fugiat nulla pariatur. Excepteur sint occaecat cupidatat non proident, sunt in culpa qui officia deserunt mollit anim id est laborum.

Appendix B

Sample Title

Lorem ipsum dolor sit amet, consectetur adipiscing elit, sed do eiusmod tempor incididunt ut labore et dolore magna aliqua. Ut enim ad minim veniam, quis nostrud exercitation ullamco laboris nisi ut aliquip ex ea commodo consequat. Duis aute irure dolor in reprehenderit in voluptate velit esse cillum dolore eu fugiat nulla pariatur. Excepteur sint occaecat cupidatat non proident, sunt in culpa qui officia deserunt mollit anim id est laborum.